

Seeds of Life in Space (SOLIS) VI. Chemical evolution of sulfuretted species along the outflows driven by the low-mass protostellar binary NGC1333-IRAS4A

V Taquet, C. Codella, Marta de Simone, Ana Lopez-Sepulcre, J. E. Pineda, Dominique Segura-Cox, C. Ceccarelli, Paola Caselli, Antoine Gusdorf, M. Persson, et al.

▶ **To cite this version:**

V Taquet, C. Codella, Marta de Simone, Ana Lopez-Sepulcre, J. E. Pineda, et al.. Seeds of Life in Space (SOLIS) VI. Chemical evolution of sulfuretted species along the outflows driven by the low-mass protostellar binary NGC1333-IRAS4A. Astronomy and Astrophysics - A&A, 2020, 637, pp.A63. 10.1051/0004-6361/201937072 . hal-02928270

HAL Id: hal-02928270
https://hal.science/hal-02928270

Submitted on 18 Dec 2020

HAL is a multi-disciplinary open access archive for the deposit and dissemination of scientific research documents, whether they are published or not. The documents may come from teaching and research institutions in France or abroad, or from public or private research centers.

L'archive ouverte pluridisciplinaire **HAL**, est destinée au dépôt et à la diffusion de documents scientifiques de niveau recherche, publiés ou non, émanant des établissements d'enseignement et de recherche français ou étrangers, des laboratoires publics ou privés.

A&A 637, A63 (2020)
https://doi.org/10.1051/0004-6361/201937072
© ESO 2020

Astronomy & Astrophysics

Seeds of Life in Space (SOLIS)

VI. Chemical evolution of sulfuretted species along the outflows driven by the low-mass protostellar binary NGC 1333-IRAS4A*

V. Taquet[1], C. Codella[1,2], M. De Simone[2], A. López-Sepulcre[2,3], J. E. Pineda[4], D. Segura-Cox[4], C. Ceccarelli[2,1], P. Caselli[4], A. Gusdorf[5,6], M. V. Persson[7], F. Alves[4], E. Caux[8], C. Favre[2], F. Fontani[1], R. Neri[3], Y. Oya[9], N. Sakai[10], C. Vastel[8], S. Yamamoto[9], R. Bachiller[11], N. Balucani[12,1,2], E. Bianchi[2], L. Bizzocchi[4], A. Chacón-Tanarro[11], F. Dulieu[13], J. Enrique-Romero[2], S. Feng[14,15], J. Holdship[16], B. Lefloch[2], A. Jaber Al-Edhari[2,17], I. Jiménez-Serra[18], C. Kahane[2], V. Lattanzi[4], J. Ospina-Zamudio[2], L. Podio[1], A. Punanova[19], A. Rimola[20], I. R. Sims[21], S. Spezzano[4], L. Testi[22,1], P. Theulé[23], P. Ugliengo[24], A. I. Vasyunin[19,25], F. Vazart[2], S. Viti[16], and A. Witzel[2]

(Affiliations can be found after the references)

Received 7 November 2019 / Accepted 12 January 2020

ABSTRACT

Context. Low-mass protostars drive powerful molecular outflows that can be observed with millimetre and submillimetre telescopes. Various sulfuretted species are known to be bright in shocks and could be used to infer the physical and chemical conditions throughout the observed outflows.

Aims. The evolution of sulfur chemistry is studied along the outflows driven by the NGC 1333-IRAS4A protobinary system located in the Perseus cloud to constrain the physical and chemical processes at work in shocks.

Methods. We observed various transitions from OCS, CS, SO, and SO_2 towards NGC 1333-IRAS4A in the 1.3, 2, and 3 mm bands using the IRAM NOrthern Extended Millimeter Array and we interpreted the observations through the use of the Paris-Durham shock model.

Results. The targeted species clearly show different spatial emission along the two outflows driven by IRAS4A. OCS is brighter on small and large scales along the south outflow driven by IRAS4A1, whereas SO_2 is detected rather along the outflow driven by IRAS4A2 that is extended along the north east–south west direction. SO is detected at extremely high radial velocity up to +25 km s^{-1} relative to the source velocity, clearly allowing us to distinguish the two outflows on small scales. Column density ratio maps estimated from a rotational diagram analysis allowed us to confirm a clear gradient of the OCS/SO_2 column density ratio between the IRAS4A1 and IRAS4A2 outflows. Analysis assuming non Local Thermodynamic Equilibrium of four SO_2 transitions towards several SiO emission peaks suggests that the observed gas should be associated with densities higher than 10^5 cm^{-3} and relatively warm ($T > 100$ K) temperatures in most cases.

Conclusions. The observed chemical differentiation between the two outflows of the IRAS4A system could be explained by a different chemical history. The outflow driven by IRAS4A1 is likely younger and more enriched in species initially formed in interstellar ices, such as OCS, and recently sputtered into the shock gas. In contrast, the longer and likely older outflow triggered by IRAS4A2 is more enriched in species that have a gas phase origin, such as SO_2.

Key words. astrochemistry – ISM: abundances – ISM: molecules – stars: formation – ISM: jets and outflows – ISM: individual objects: NGC 1333-IRAS4A

1. Introduction

The early stages of low-mass star formation are accompanied by the detection of bright bipolar low-velocity (typically ~10 km s^{-1}) outflows on scales as large as several thousands of astronomical units (au). These outflows can be produced by fast (~100 km s^{-1}) protostellar jets, which in turn form shocks upon impact against the high-density protostellar gas. In addition, slower disc winds can also contribute in sweating up material. More specifically, Tabone et al. (2017) recently showed that SO and SO_2 emission as observed towards the HH212 protostar traces outflowing material launched by a region extended as the radius of the protostellar disc.

Shocks are favourable regions to study how the chemical content of star forming regions is enriched thanks to sputtering (gas-grain collisions) and shattering (grain-grain) processes (Draine & Salpeter 1979; Tielens et al. 1994; Flower & Pineau des Forets 1994; Guillet et al. 2007). In practice, the components of both dust mantles and refractory cores are injected into the gas. In addition, the sudden increases of temperature and density trigger a hot gas-phase chemistry otherwise not efficient in more quiescent regions. As a consequence, the abundance of several molecular species dramatically increase by several orders of magnitude (Bachiller et al. 2001; Herbst, & van Dishoeck 2009).

Ground-based or space infrared-(sub-)millimetre single-dish telescopes have been used for a few decades to probe the

* Moment 0, 1, and 2 maps are only available at the CDS via anonymous ftp to cdsarc.u-strasbg.fr (130.79.128.5) or via http://cdsarc.u-strasbg.fr/viz-bin/cat/J/A+A/637/A63

large-scale formation and evolution of molecular outflows through the emission of bright species, such as CO, H_2O, NH_3, or CH_3OH, the main species of interstellar ices (e.g. Bachiller et al. 1995a, 2001; Codella & Bachiller 1999; Codella et al. 2005, 2010; Nisini et al. 2010; Kristensen et al. 2012; Yıldız et al. 2012; Busquet et al. 2014; Lefloch et al. 2017). On the other hand, interferometry is the way to image the small (down to ∼1″) regions chemically enriched due to the passage of a shock. In this context, a large number of studies have revealed bow shocks and cavities opened by protostellar jets (Gueth et al. 1998; Bachiller et al. 1998b; Benedettini et al. 2007, 2013; Codella et al. 2009, 2017; Persson et al. 2012; Santangelo et al. 2015; Lefèvre et al. 2017).

Many species showing a strong increase of their abundance in shocks along low-mass protostellar outflows are sulfuretted. It has been assumed that H_2S is the main reservoir of sulfur in the dust mantles, its release in the gas phase through sputtering or thermal evaporation would then trigger the formation of gaseous SO followed by SO_2 (Pineau des Forets et al. 1993; Charnley 1997). In other words, the H_2S/SO/SO_2 abundance ratios have been proposed as chemical clocks of the shocked gas. Unfortunately, the comparison with observations of S-bearing species along outflows did not provide any clear result in this context (Codella & Bachiller 1999; Wakelam et al. 2004). In addition, so far H_2S has not been detected in interstellar ices (e.g. Boogert et al. 2015, and references therein) questioning this hypothesis and calling for alternative possibilities. Wakelam et al. (2004) proposed that the sulfur released from dust mantles is in atomic form. On the other hand, OCS could be the solution. Although also OCS has been only tentatively detected on ices (Boogert et al. 2015), astrochemical models interpreting molecular surveys towards protostellar shocks along the outflow driven by the L1157-mm Class 0 protostar (hereinafter L1157) suggest that OCS represents at least 50% of the sulfur reservoir in ice mantles (Podio et al. 2014; Holdship et al. 2016). All these findings call for more comprehensive datasets to shed light on the sulfuretted grain/ice composition. A first step has been done by Holdship et al. (2018), who analysed the unbiased spectral survey towards again L1157 performed with the IRAM-30 m in the context of the Astrochemical Surveys At IRAM (ASAI) Large Program (Lefloch et al. 2018): more than 100 lines have been associated with the following molecules CCS, H_2CS, OCS, SO, SO_2, and H_2S (from Holdship et al. 2016) and collecting 10% of the cosmic sulfur abundance. It is time to perform a multiline analysis of sulfuretted species using interferometric data (to minimise filling factor effects) and towards other outflows than L1157 in order to check that the L1157, a chemicallly rich outflow, does not represent a unique case.

NGC 1333-IRAS4A (hereinafter IRAS4A) is a protobinary system located in the NGC 1333 star-forming region of the Perseus cloud (299±15 pc; Zucker et al. 2018) with a systemic velocity of 7 km s^{-1} (Yıldız et al. 2012). The two Class 0 protostars are separated by 1.″8 (538 au; see e.g. Looney et al. 2000; López-Sepulcre et al. 2017; Tobin et al. 2018) and surrounded by an 8 $M_\odot$ envelope (Maury et al. 2019). IRAS4A is one of the brightest known low-mass protostellar systems, with an overall internal luminosity of ∼5 $L_\odot$ (Maury et al. 2019), measured in the context of the *Herschel* Gould Belt survey (see e.g. André et al. 2010; Ladjelate et al. 2020).

The two protostars have different characteristics: the SE source, called 4A1, shows the brightest mm-continuum emission, but it does not show any signature of chemically enriched protostellar cocoon whilst the NW protostar, 4A2, is associated with a hot-corino detected through various complex organic molecules (Bottinelli et al. 2004, 2007; Taquet et al. 2015; Santangelo et al. 2015; López-Sepulcre et al. 2017). The binary protostellar system drives two bipolar outflows observed on large scales (few arcminutes). Choi (2005) mapped the outflows in SiO emission, mainly induced by the sputtering of refractory grains (e.g. Caselli et al. 1997; Gusdorf et al. 2008a,b, and references therein), at 2″ spatial resolution. Two different blue-shifted lobes are clearly observed towards South: more specifically, one along South and one towards south west. The northern lobe, as traced by Choi (2005), shows only one lobe, which is abruptly bending toward north-west once at 20″ (6000 au) from the protostars. Using IRAM-PdBI observations of CO, SO, and SiO lines with a spatial resolution of 300 au, Santangelo et al. (2015) were able to reveal two protostellar jets: a fast jet associated with H_2 shocked emission and driven by 4A1 (south lobe) and a slower and precessing jet emerging from 4A2 (SW). The northern red-shifted counterparts are not clearly disentangled even at interferometric scale. Interestingly, interferometric CO images obtained with the SMA by Ching et al. (2016) suggest that the magnetic field is wrapping the two northern red-shifted components. However, the complex red-shifted emission is far to be well revealed and imaged. This is crucial because the jet/outflow properties can be used to date the different evolutionary stages of the two protostars. In practice, due to its fainter continuum emission, and its richer chemistry, 4A2 is thought to be older than 4A1. This picture is consistent with the more elongated outflow driven by 4A2 along the north east-south west (NE–SW) direction relative to the outflow driven by 4A1 towards south.

Here, we aim at analysing the emission of various transitions from four sulfuretted molecules, namely OCS, SO, SO_2, and CS with different excitation ranges and on different spatial scales along the outflows of IRAS4A. An atomic sulfur abundance of $1-4 \times 10^{-7}$ towards the south outflow of IRAS4A has been estimated by Anderson et al. (2013) from S[I] observations at 25 μm with *Spitzer*. We use interferometric observations taken in the context of the SOLIS (Ceccarelli et al. 2017, Seeds Of Life In Space) IRAM Northern Extended Millimeter Array (NOEMA) Large Program, supported by further interferometric datasets. The goal of this Large Program is to study the organic (and sulfuretted) molecular content in a sample of low-mass star-forming regions in different stages and environments. The spatial evolution of organic molecules along the outflows driven by IRAS4A is presented in a parallel and complementary study by De Simone et al. (2019). The goal of the paper is twofold: (1) to derive for the first time the physical conditions of the IRAS4A outflows, so far observed only using individual transitions of CO, SO, and SiO, and to disentangle the red-shifted northern components; (2) to investigate the evolution of the chemical conditions, using also up-to-date physical/chemical models of shocked regions, along the two outflows driven by IRAS4A.

2. Observations

We make use of various Plateau de Bure Interferometer (PdBI) and NOrthern Extended Millimeter Array (NOEMA) datasets from four observational programs in the 1.3, 2, and 3 mm bands and at different configurations. The properties of the transitions targeted in this work are summarised in Table 1.

For the SOLIS data, the IRAS4A binary system was observed in three different Setups (1, 3, and 5) with the IRAM NOEMA interferometer during several tracks in June and September 2016 (see Table 1 of Ceccarelli et al. 2017). Setup 1, 3, and 5 cover the frequency ranges from 80.8 to 84.4 GHz, from 95.7 to 99.5 GHz, and between 204.0 and 207.6 GHz, respectively. For Setups 1 and 3, the array was used in both

Table 1. Properties of the transitions presented in this work.

Molecule	Transition	Frequency (GHz)	E_{up} (K)	A_{ul} (s^{-1})	θ_{beam} ($'' \times ''$)	Dataset	rms noise (blue) (Jy $beam^{-1}$)	rms noise (red) (Jy $beam^{-1}$)
OCS	8−7	97.301209	21.0	2.58(−6)	2.2 × 2.0	SOLIS-S3	7.40(−3)	5.57(−3)
$OC^{34}S$	7−6	83.057970	15.9	1.59(−6)	4.3 × 3.4	SOLIS-S1	5.70(−3)	5.80(−3)
OCS	17−16	206.745155	89.3	2.55(−5)	0.9 × 0.7	SOLIS-S5	1.53(−2)	1.18(−2)
OCS	18−17	218.903355	99.8	3.03(−5)	0.8 × 0.7	CALYPSO	2.00(−2)	1.73(−2)
CS	2−1	97.980953	7.1	1.67(−5)	2.2 × 2.0	SOLIS-S3	2.00(−1)	1.00(−1)
$C^{34}S$	2−1	96.41295	6.2	1.60(−5)	2.2 × 2.0	SOLIS-S3	1.06(−2)	5.50(−3)
$C^{34}S$	3−2	144.617109	11.8	5.78(−5)	2.1 × 1.7	T15	3.76(−2)	3.68(−2)
SO	3_2−2_1	99.299870	9.2	1.12(−5)	2.2 × 2.0	SOLIS-S3	7.90(−2)	4.20(−2)
^{34}SO	3_2−2_1	97.715317	9.1	1.07(−5)	2.2 × 2.0	SOLIS-S3	5.10(−3)	4.30(−3)
SO	6_5−5_4	219.949442	35.0	1.36(−4)	0.8 × 0.7	CALYPSO	9.50(−2)	8.40(−2)
SO	4_5−3_4	206.176005	38.6	1.00(−4)	0.9 × 0.7	SOLIS-S5	2.40(−2)	2.30(−2)
SO_2	$5_{2,4}$−$5_{1,5}$	165.144651	23.6	3.12(−5)	2.4 × 1.8	T15	4.90(−2)	5.30(−2)
SO_2	$7_{1,7}$−$6_{0,6}$	165.225452	27.1	4.13(−5)	2.4 × 1.8	T15	7.30(−2)	9.60(−2)
SO_2	$8_{1,7}$−$8_{0,8}$	83.688093	36.7	6.83(−6)	4.3 × 3.4	SOLIS-S1	1.20(−2)	1.05(−2)
SO_2	$11_{2,10}$−$11_{1,11}$	205.300570	70.2	5.31(−5)	0.9 × 0.7	SOLIS-S5	8.70(−3)	5.30(−2)
SO_2	$13_{2,12}$−$13_{1,13}$	225.153703	93.0	6.52(−5)	1.1 × 0.8	P12	4.02(−2)	3.29(−2)
SO_2	$14_{1,13}$−$14_{0,14}$	163.605530	101.8	3.01(−5)	2.4 × 1.8	T15	3.40(−2)	5.50(−2)
SO_2	$16_{2,14}$−$16_{1,15}$	143.057110	137.5	3.57(−5)	2.1 × 1.7	T15	2.30(−2)	2.50(−2)
SiO	5−4	217.104980	31.3	5.21(−4)	1.1 × 0.8	CALYPSO	9.58(−2)	1.20(−1)
CH_3OH	$3_{1,3}$−$2_{1,2}$, A	143.865795	28.3	1.07(−5)	2.2 × 1.8	T15	9.60(−2)	4.10(−2)
NH_3	3, 3	23.870129	123.5	2.58(−7)	2.0 × 2.0	C07	3.10(−3)	2.80(−3)

Notes. SOLIS-S1, -S3, and -S5 stand for Setups 1, 3, and 5 of the SOLIS data, respectively (see text for more details). C07, P12, and T15 stand for Choi et al. (2007), Persson et al. (2012), and Taquet et al. (2015), respectively.

configurations D and C with baselines from 16 to 240 m for Setup 1 and from 15 to 304 m for Setup 3. For Setup 5, the array was used in configurations A and C. The phase centre is on the IRAS4A1 source, α(J2000) = $03^h29^m10\overset{s}{.}5$, δ(J2000) = +31°13′30.″9. The bandpass was calibrated on 3C454.3 and 3C84, the absolute flux was fixed by observing MWC349, LKHA101, 2013+370, and 2007+659, and 0333+321 was used to set the gains in phase and amplitude. The final uncertainty on the absolute flux scale is ≤15%. The phase rms was ≤50°, the typical precipitable water vapour (pwv) was from 4 to 15 mm, and the system temperatures ranged typically between 50 and 200 K. The data were reduced using the packages CLIC and MAPPING of the GILDAS[1] software collection. A continuum map was obtained by averaging line-free channels and self calibrating the data. The self calibration solutions were then applied to the spectral cube, which was subsequently cleaned. The resulting synthesised FWHM beam is 4.″5×3.″5 (PA = 27°) for Setup 1, 2.″2 × 1.″9 (PA = 96°) for Setup 3, and 0.″9 × 0.″7 (PA = 47°) for Setup 5. The half power primary beam is 61.″4, 59.″2, and 24.″5 for Setups 1, 3, and 5 respectively.

We used the CALYPSO data observed with the IRAM-PdBI (Maury et al. 2019) to extract the interferometric maps from the SiO(5−4), SO(6_5−5_4), and OCS(8−7) transitions at ∼218 GHz. These observations were carried out between February 2011 and February 2013 as part of the CALYPSO Large Program using the A and C configurations of the array. The synthesised FWHM beam at 1.4 mm is 1.″1 × 0.″8. More details on the observational properties can be found in Santangelo et al. (2015).

IRAS4A was observed with the IRAM PdBI at 145 and 165 GHz on 2010 July 20, 21, August 1, 3, November 24, and 2011 March 10 in the C and D most compact configurations of the array. The baseline range of the observations is 25–140 m, allowing us to recover emission on scales from 10–15″ to ∼2″. The WIDEX backends have been used at 143.4 and 165.2 GHz, providing a bandwidth of 3.6 GHz each with a spectral resolution of 1.95 MHz (∼3.5–4 km s^{-1}). High-resolution narrowband backends focused on two CH_3OH lines have also been used. They provide a bandwidth of 80 MHz with a spectral resolution of 0.04 MHz (0.08 km s^{-1}). We decreased the spectral resolution to 0.40 MHz (0.8 km s^{-1}) to obtain a better signal-to-noise. More details on the observational dataset can be found in Taquet et al. (2015).

PdBI observations at 225 GHz were performed on 27 and 28 November 2011, on 12, 15, 21, 27 March 2012, and on 2 April 2012 in the B and C configurations of the array. The synthesised FWHM beam is 1.″2×1.″0. A more detailed description of the observational setups is provided by Persson et al. (2014).

For all datasets, the amplitude calibration uncertainty is estimated to be ∼15−20%. Given we map relatively extended structures such as outflow lobes, we cleaned the images using the Hogbom method with natural weighting and with a mask containing all the molecular lobes to minimise artefacts in the cleaned image.

3. Results

3.1. Spatial distribution

Integrated intensity maps from various sulfuretted transitions observed at 1″ (hereafter called high) and about at 2–4″ (hereafter called low) angular resolutions are shown in Fig. 1. "Zoomed" maps around the IRAS4A protobinary system of the

[1] http://www.iram.fr/IRAMFR/GILDAS/

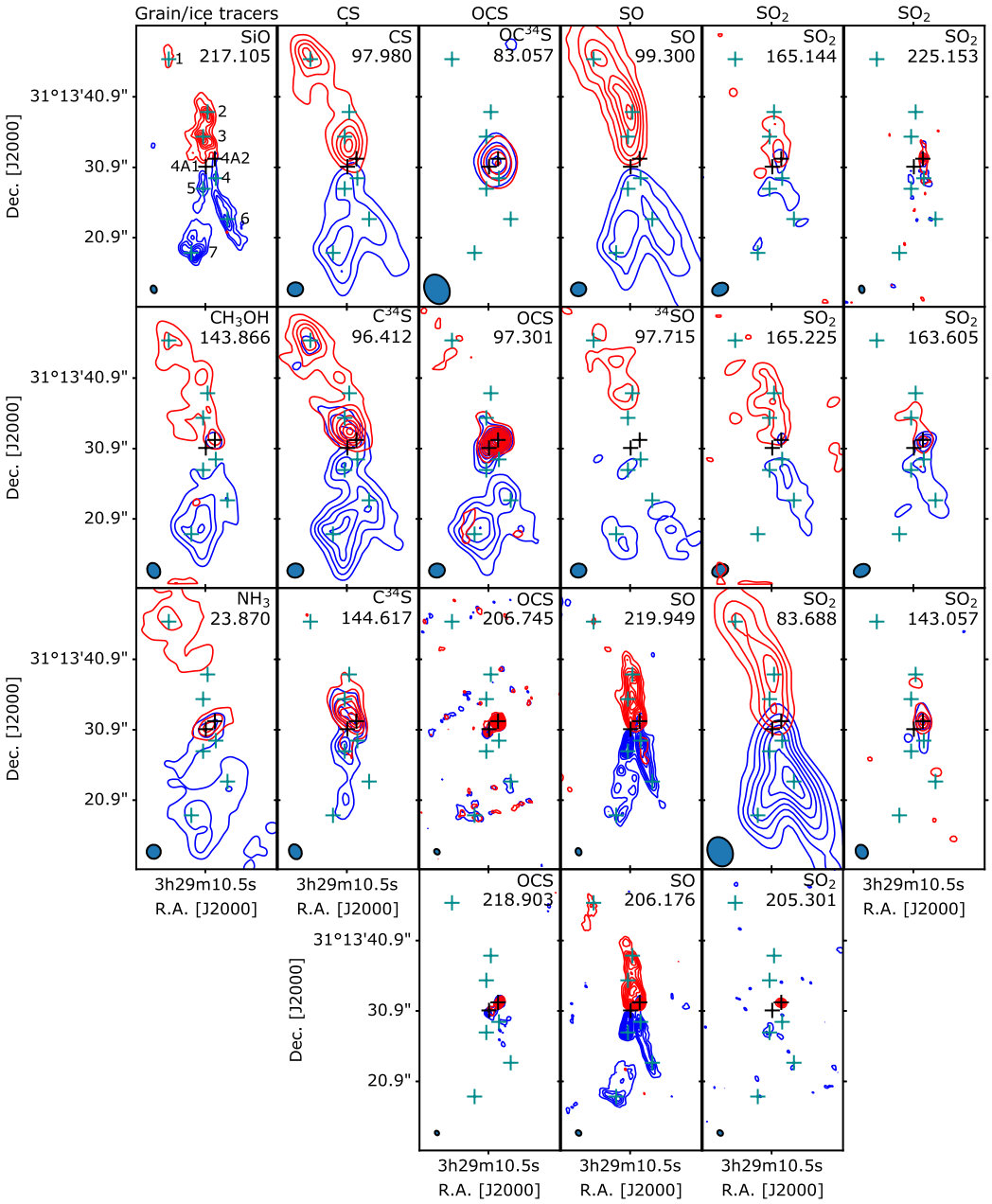


Fig. 1. Moment 0 integrated maps of the transitions from SiO, CH_3OH, NH_3, CS, OCS, SO, and SO_2 integrated over the (−10, +7) km s^{-1} (blue) and (+7, 30) km s^{-1} (red) ranges. Contour levels increase in steps of 3σ, the σ noise levels of each map are listed in Table 1. Transition frequency (in GHz) is given at the top right of each panel. Black crosses represent the position of the 4A1 and 4A2 sources of the IRAS4A binary system. Green crosses represent the position of the SiO(5–4) emission peaks along the outflows.

transitions observed at "high" angular resolution are also shown in Fig. 2. For comparison, we also show the emission from SiO(5−4), NH_3(3, 3), and A-$CH_3OH(3_{1,3}-2_{1,2})$ transitions. The SiO(5−4) has been observed as part of the CALYPSO Large Program at ∼1″ resolution and was presented in Santangelo et al. (2015). The A-$CH_3OH(3_{1,3}-2_{1,2})$ transition at 143.866 GHz observed at ∼2″ was presented in Taquet et al. (2015). A more detailed analysis of the CH_3OH emission along the outflows driven by IRAS4A is presented in a complementary study (De Simone et al. 2019). The NH_3(3, 3) emission was observed by Choi et al. (2007) with the VLA interferometer with a ∼2″ resolution. SiO is thought to be formed in the gas phase from Si atoms initially locked at ∼90% in refractory grains and then sputtered in shocks whilst methanol CH_3OH and ammonia NH_3 are two abundant ice components. Methanol in particular is only formed at the surface of interstellar ices and cannot form efficiently through gas phase chemistry (Watanabe & Kouchi 2002; Geppert et al. 2006). Since methanol should be efficiently destroyed in the hot (T > 2000 K) gas, it would therefore indicate the location of shock fronts where ice has been recently sputtered. SiO, NH_3, and CH_3OH can be therefore considered as reference species to locate the position of shocks throughout the outflows. The positions of the SiO(5−4) emission peaks along the outflows are depicted by the green crosses with associated peak numbers.

It can be clearly noticed that OCS, SO, and SO_2 targeted at high angular resolution trace different regions of the protostellar outflows. The blue emission of the SiO(5−4) and the two SO

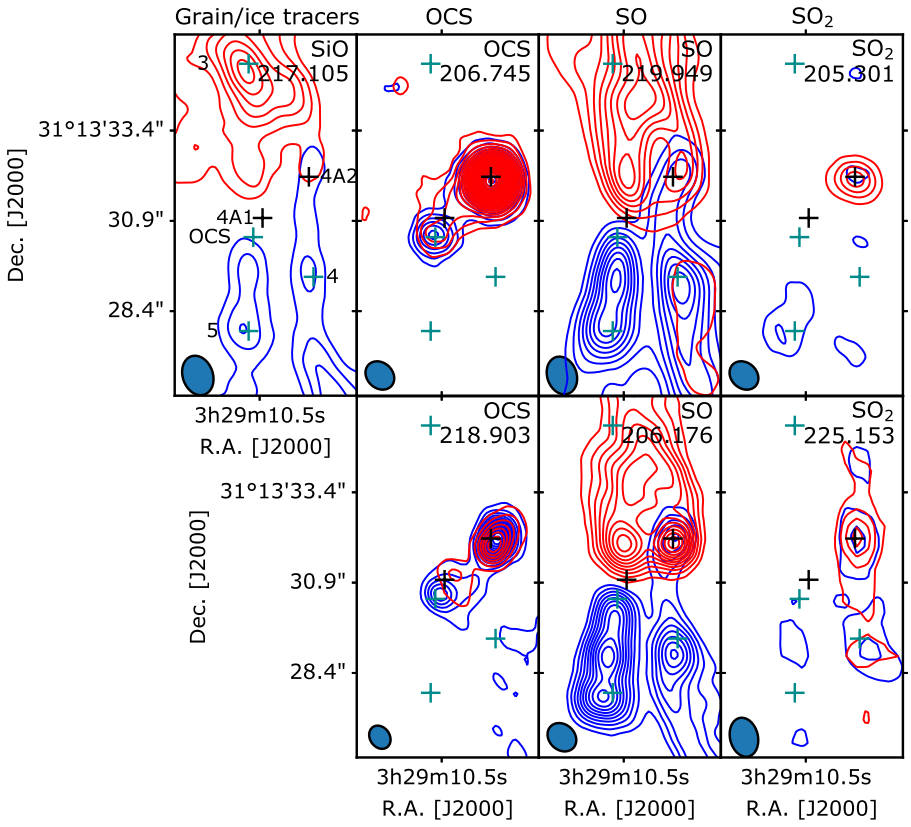


Fig. 2. Moment 0 integrated maps zoomed around the IRAS4A protostellar system of the transitions from SiO, OCS, SO, and SO_2 observed at high (~1″) angular resolution integrated over the (−10, +7) km s^{-1} (blue) and (+7, 30) km s^{-1} (red) ranges. Contour levels increase in steps of 3σ, the σ noise levels of each map are listed in Table 1. Transition frequency (in GHz) is given at the top right of each panel. Black crosses represent the position of the 4A1 and 4A2 sources of the IRAS4A binary system. Green crosses represent the position of the SiO(5–4) and the blue OCS emission peaks along the outflows.

transitions clearly allows us to disentangle the outflow emission from the two sources IRAS4A1 and A2. The outflow driven by IRAS4A1 seems to extend along the south-north (hereafter S–N) direction whilst the outflow driven by IRAS4A2 extends along the south west–north east (hereafter SW–NE) direction. The SO(4_5−3_4) transition at 206.176 GHz of our SOLIS data observed at high angular resolution therefore confirms the CALYPSO results already shown by Santangelo et al. (2015).

Unlike SO, OCS shows its brightest emission towards the hot corino of IRAS4A2. Interestingly, another OCS emission peaking at +3 km s^{-1} is also detected at (+0.2″, −0.4″) with respect to 4A1 for the two targeted transitions and its position is depicted in the SiO map in Fig. 2. The location of this second OCS peak corresponds to the beginning of the south outflow driven by 4A1 detected in SO and SiO. The SO_2 transition shows extended emission but mostly in the blue range, around SiO peak 5 for the $11_{2,10}$−$11_{1,11}$ transition at 225.301 GHz and around SiO peak 4 for the $13_{2,12}$−$13_{1,13}$ one at 205.300 GHz.

At large scales, extended emission from OCS is only detected in the blue (i.e. V < 7 km s^{-1}) component, with a bright emission peak in the south outflow around SiO peak 7 driven by source 4A1 and a second fainter emission peak near SiO peak 6 along the NW–SE outflow. SO and CS show extended emission in the blue and red components along the SW–NE and the south outflow with relatively similar intensities. For SO, the red component emission peaks follow SiO peaks 1, 2, and 3 whilst the blue component peaks are located near SiO peaks 5, 6, and 7. CS, on the other hand, does not show any bright emission near SiO peak 2. SO_2 is brighter along the SW–NE outflow. In fact, SO_2 transitions at 143, 165, and 225 GHz are only detected along the SW–NE outflow, but the $8_{1,7}$−$8_{0,8}$ transition at 83.688 GHz also extends towards the south lobe driven by 4A1.

In order to compare the spatial distribution of the targeted molecules, we list in Table 2 the Spearman[2] ranking correlation coefficients of the blue and red emissions from the sulfuretted and methanol transitions observed at "low" angular resolution. To compute the "blue" ("red") coefficients between two given transitions, we included pixels where the "blue" ("red") integrated emissions of both transitions are higher than the 4σ noise level. We verified that modifying the detection threshold between 3σ and 5σ for including the pixels in the coefficient estimation induces a variation of the Spearman coefficients by typically 20% at most. Sets of transitions with Spearman coefficients higher than 0.6 can be considered as strongly correlated whilst transitions with Spearman coefficients lower than 0.4 are considered as uncorrelated. Since the "red" emission of the OCS transition is not detected along outflows, the corresponding Spearman coefficients are not included. As previously noted at first glance, the "blue" emission of OCS does not show any correlation with other sulfuretted species, with coefficients lower than 0.3, but seems to correlate relatively well with CH_3OH. SO_2 and SO seem to strongly correlate together with a coefficient higher than 0.8 for both emissions. The "blue" emission from CS seems to correlate well with SO and SO_2, with a coefficient higher than 0.6, confirming our first visual impression. However, the coefficients between the "red" CS emission and the "red" SO and SO_2 emissions are lower than 0.25. Indeed, CS is only bright near SiO peaks 1 and 3 whereas SO and SO_2 emissions also peak near SiO peak 2.

To summarise, OCS, CS, SO, and SO_2 clearly show different spatial emission along the two outflows driven by IRAS4A. On large scales, OCS is brighter in the south outflow driven

[2] The Spearman correlation coefficient is defined as the Pearson correlation coefficient between the rank variables, they are consequently less affected by outliers.

Table 2. Spearman's rank correlation coefficients between the "blue" and "red" integrated emissions of molecules observed at low angular resolution.

	CH_3OH $(3_{1,3}-2_{1,2})$ Blue/Red	OCS (8−7) Blue/Red	CS (2−1) Blue/Red	SO (3_2-2_1) Blue/Red	SO_2 $(8_{1,7}-8_{0,8})$ Blue/Red
$CH_3OH(3_{1,3}-2_{1,2})$	1/1	0.61/ -	0.77/0.26	0.34/0.20	−0.08/0.21
OCS(8−7)	0.61/ -	1/1	0.27/ -	0.09/ -	0.14/ -
CS(2−1)	0.77/0.26	0.27/ -	1/1	0.66/0.01	0.66/0.24
$SO(3_2-2_1)$	0.34/0.20	0.09/ -	0.66/0.01	1/1	0.83/0.84
$SO_2(8_{1,7}-8_{0,8})$	−0.08/0.21	0.14/ -	0.66/0.24	0.83/0.84	1/1

Notes. Left and right values correspond to the Spearman's rank correlation coefficients obtained for the "blue" and "red" emissions, respectively, when the emissions from both considered transitions are higher than the 4σ noise level.

by IRAS4A1 whereas SO_2 is rather detected along the outflow driven by IRAS4A2 extended along the NE–SW direction. CS and SO show extended emission along the two outflows. On smaller scales, an OCS emission peak is detected close to the launching region of the south outflow driven by 4A1 detected in SO and SiO.

3.2. Opacity estimates

We detected extended emission of the CS(2−1) and $SO(3_2-2_1)$ transitions from the two ^{32}S and ^{34}S isotopologues with similar observational properties. The emission maps therefore allow us to estimate the opacities of the main ^{32}S transitions, τ_{32}, towards each pixel of the map. Assuming optically thin emission from the ^{34}S isotopologues, a local thermodynamic equilibrium (LTE) population of the levels, and same rotational temperature $T_{\rm rot}$ for both isotopologues, τ_{32} can be derived from the following formula (see Goldsmith & Langer 1999, for more details)

$$\frac{\tau_{32}}{1-\exp(-\tau_{32})} = \left(\frac{N_{32}}{N_{34}}\right)\times\left(\frac{Z_{34}}{Z_{32}}\right)\times\left(\frac{\nu_{34}}{\nu_{32}}\right)^2\times\left(\frac{A_{\rm u,l,32}}{A_{\rm u,l,34}}\right)\times\left(\frac{g_{\rm up,32}}{g_{\rm up,34}}\right) \times\left(\frac{W_{34}}{W_{32}}\right)\times\exp\left(\frac{E_{\rm up,34}-E_{\rm up,32}}{kT_{\rm rot}}\right) \quad (1)$$

where $\left(\frac{N_{32}}{N_{34}}\right)$ is the column density ratio between the ^{32}S and ^{34}S isotopologues of each species, assumed to be equal to the elemental $^{32}S/^{34}S$ ratio of 22 in the local interstellar medium (Wilson & Rood 1994); Z, ν, $A_{\rm u,l}$, $g_{\rm up}$, W, and $E_{\rm up}$ are the partition functions at a given $T_{\rm rot}$, the frequency, the Einstein-A coefficient, the statistical weight, the integrated brightness temperature, and the upper level energy of the (^{32}S or ^{34}S) transition, respectively. We then numerically interpolated the opacity τ_{32} from the left term of Eq. (1) towards each pixel of the map if the intensity of the ^{32}S and ^{34}S are both higher than the 4σ noise level.

Figure 3 shows the opacity maps of the CS(2−1) and $SO(3_2-2_1)$ transitions for $T_{\rm rot}$ = 30 K. It should be noted that the results do not significantly depend on the assumed value of $T_{\rm rot}$ as long as $T_{\rm rot}$ is higher than 10 K, due to the similar upper level energies between the transitions of the ^{32}S and ^{34}S isotopologues (differences of 0.9 and 0.1 K for CS and SO, respectively). Opacity errors induced by the flux calibration uncertainties are about 30%. It can be seen that the CS(2−1) transition is moderately optically thick with $\tau\sim1$ throughout most of the outflows and shows an opacity higher than 2 close to source 4A2. In contrast, $SO(3_2-2_1)$ is optically thin with $\tau<<1$ in most of the outflows.

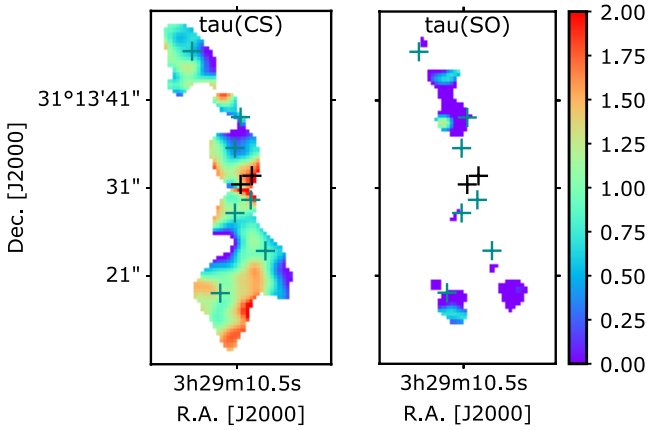


Fig. 3. Opacity maps of the CS(2−1) and $SO(3_2-2_1)$ transitions estimated from the intensity ratio of the ^{32}S and ^{34}S transitions when the flux of both isotopologues is higher than four times the σ rms noise level and assuming the ^{34}S transitions are optically thin (see text for more details). Black crosses represent the position of the 4A1 and 4A2 sources of the IRAS4A binary system. Green crosses represent the position of the SiO(5–4) emission peaks along the outflows.

3.3. Kinematics along the outflows

Figure 4 presents the moment 1 and moment 2 maps of SiO and the sulfuretted transitions observed at "high" and "low" angular resolutions. As supporting material, Figs. A.1 and A.2 present the velocity emission maps whilst Figs. B.1 and B.2 show the spectra of the sulfuretted species obtained towards the SiO and the OCS emission peaks depicted in the SiO maps in Figs. 1 and 2.

The moment 1 and moment 2 maps at "high" angular resolution of SiO and SO clearly allow us to disentangle the two components of the molecular outflows both in the north and the south parts. In the northern part, the outflow driven by 4A1 is much faster with a velocity peak of ∼30 km s^{-1} and a velocity linewidth of ∼25 km s^{-1}, both seen in SiO and SO. On the other hand, the outflow driven by IRAS4A2 seems to be slower, with a peak velocity of ∼20 km s^{-1} and a velocity linewidth of ∼10 km s^{-1} for both molecules. In the southern part, the S–N outflow driven by 4A1 is slightly faster with a peak velocity of approximately −5 km s^{-1} (or ∼12 km s^{-1} relative to the source velocity) whereas the SW outflow driven by 4A2 has a peak velocity of ∼0−5 km s^{-1}.

The low angular resolution maps are obtained at lower frequency, between 80 and 100 GHz, decreasing the velocity

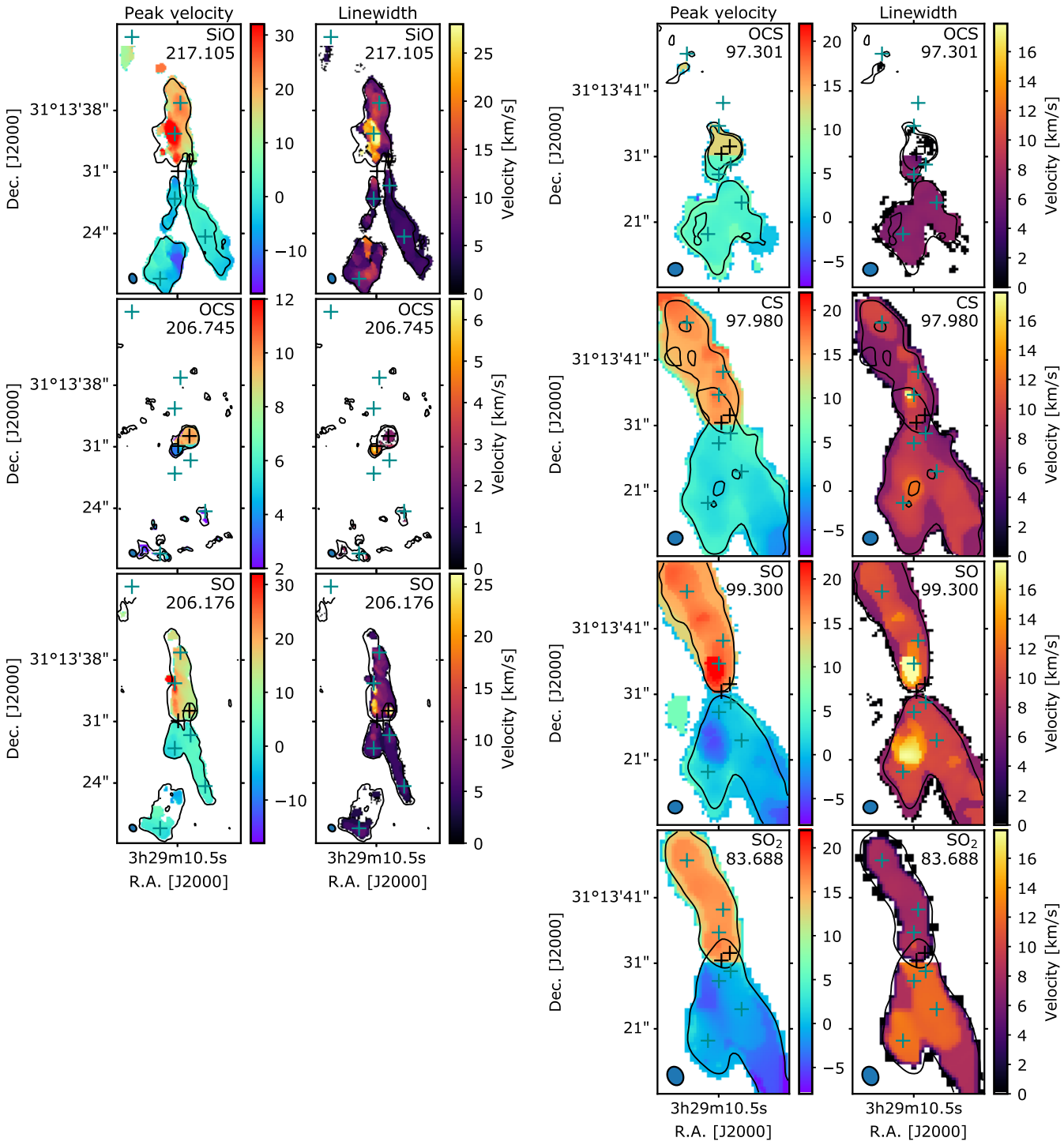


Fig. 4. Moment 1 and moment 2 maps of the SiO(5−4), OCS(17−16), and SO(6_5−5_4) emission observed at "high", 1″, angular resolution (*left panels*) and of the OCS(8−7), SO(3_2−2_1), CS(2−1), and SO_2($8_{1,7}$−$8_{0,8}$) emission at "low", 2−4″, resolution (*right panels*). Contours represent the 3σ level. Black crosses represent the position of the 4A1 and 4A2 sources of the IRAS4A binary system. Green crosses represent the position of the SiO(5–4) emission peaks along the outflows.

resolution by a factor of ∼2.5 with respect to the high angular resolution maps at 215−220 GHz (∼6 vs. ∼2.5 km s^{-1}). Nevertheless, the low angular resolution moment maps of SO(3_2−2_1) also reveal high velocity emission associated with the S–N outflow driven by 4A1, with peak velocities of +20 and −5 km s^{-1} in the north and south, respectively, and velocity linewidth of 15 km s^{-1}, confirming the high angular resolution maps. The low velocity resolution of the low-angular resolution maps prevents us to detect any weaker evolution of the velocity along the outflows for the other species.

3.4. Comparison with the IRAM-30 m spectra

In order to estimate the flux resolved out by the NOEMA interferometer, we compared the spectra obtained with our NOEMA datasets with the single-dish spectra obtained with the

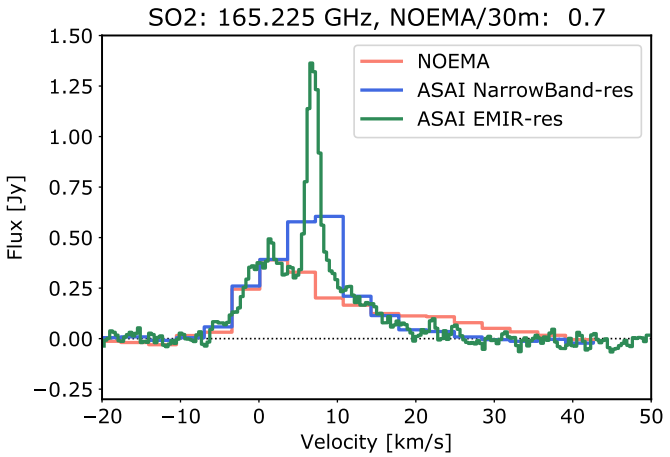


Fig. 5. Flux spectra of SO_2 at 165.225 GHz observed with the IRAM-30 m with the ASAI Large Program with the EMIR spectral resolution (in green) and smoothed over the WIDEX resolution (in blue) and with the NOEMA interferometer assuming a mask equal to the IRAM-30 m beam (in red). The flux recovered by NOEMA is reported on top of the panel (see text in Sect. 3.4 for more details).

IRAM-30 m single-dish telescope as part of the ASAI Large Program (Lefloch et al. 2018). Briefly, the aim of the ASAI program was to carry out an unbiased spectral survey at high spectral resolution of a sample of young nearby low-mass and intermediate-mass protostars in the 3, 2, and 1.3 mm spectral windows. To obtain the NOEMA spectra, we estimated the flux of each spectral channel coming from a circular mask of a size equal to the beam of the IRAM-30 m telescope that ranges from ∼30″ at 80 GHz to ∼10″ at 220 GHz.

The single-dish spectra of transitions from sulfuretted molecules, SiO, and CH_3OH detected in the ASAI data are compared with the NOEMA spectra in Fig. C.1. We also show one representative transition is shown in Fig. 5, the SO_2 transition at 165.225 GHz. We present the ASAI spectra both for the original 200 kHz spectral resolution obtained with the EMIR receiver connected to the FTS backend and for a smoother spectral resolution of 1.95 MHz equivalent to the WIDEX correlator of NOEMA. The recovered flux of transitions detected in the ASAI data at 5σ are estimated from the ratio of the flux integrated between −20 and +50 km s^{-1} and are given at the top of each panel.

High-resolution spectra from ASAI can usually be decomposed into several components (see for instance Ospina-Zamudio et al. 2018, for a more detailed description of a similar dataset towards an intermediate-mass protostar): (1) a narrow line component associated with the large scale cold and quiescent envelope, (2) a broad line component associated with the outflowing gas as seen with broad wings, (3) a moderately-broad line component associated with the hot corino. Transitions with a low upper level energy, such as the OCS(8 − 7), $SO(3_2{-}2_1)$, $SO(6_5{-}5_4)$, $SO(4_5{-}3_4)$, $SO_2(8_{1,7}{-}8_{0,8})$, or $SO_2(7_{1,7}{-}6_{0,6})$ show a bright narrow line component observed with the IRAM-30 m but not detected with NOEMA. This suggests that the cold extended emission is completely resolved out by the NOEMA interferometer with the used configurations of the array. The velocity profiles of the moderately-broad and broad components for the SO, SO_2, CH_3OH transitions show a very good agreement between the IRAM-30 m and NOEMA datasets, confirming that the high-velocity gas is associated with compact emission. The fluxes recovered by NOEMA typically range from ∼25−50% for transitions showing a bright narrow line component to ∼100% (±20% of calibration and statistical errors) for species mostly associated with compact gas.

3.5. Dissecting the molecular outflows with clustering methods

The independent analysis of the moment 0 maps, namely the integrated intensity maps of the molecular emission, and then the kinematics information included in the moment 1 and 2 maps already allowed us to distinguish by eye several components along the two molecular outflows driven by the IRAS4A protobinary system. We now aim to combine the information included in the three types of moment maps in order to quantitatively distinguish the spatial components included in the outflows through the use of a clustering method. Among the variety of clustering methods found in the literature, we chose the relatively simple and commonly used K-means algorithm (Lloyd 1982) available within the `scikit-learn` Python package. Our data are a set of pixels each characterised by two sky coordinates and $3 \times N_{\rm species}$ (integrated intensity, velocity peak, and linewidth for each species) features. The clustering algorithm only uses the molecular emission information for clustering the outflows, ignoring their spatial coordinates. Before performing the clustering analysis, we normalised the data so all features have the same mean and standard deviation. Briefly, K-means, also called Lloyd's algorithm, tries to decompose a set of N samples (i.e. here the pixels) into K disjoint clusters each described by a mean, also called centroid, by minimising their inertia, or within-cluster sum of criterion. In practice, the K-means algorithm has three steps: (1) K-Means first chooses the initial centroids. Here we employed the so-called "k-means++" initialisation scheme (David & Vassilvitskii 2007) in order to chose initial centroids that are distant from each other. (2) The algorithm then assigns each sample to its nearest centroid, namely the one with the shortest distance. (3) K-Means then creates new centroids by taken the mean value of all of the samples assigned to each previous centroid. The difference between the old and the new centroids are computed and the algorithm repeats the last two steps until this value is less than a given threshold.

We tried to apply this clustering method to the $SiO(5{-}4)$, $SO(4_5{-}3_4)$, and OCS(17−16) molecular emission observed at high angular resolution, and to the OCS(8−7), $SO(3_2{-}2_1)$, CS(2−1), and $SO_2(8_{1,7}{-}8_{0,8})$ emission at "low" resolution. However, the velocity resolution of the low-angular resolution maps is relatively low (∼6−7 km s^{-1}) resulting in only a few discrete velocity peak and linewidth values that cannot be quantitatively used for correctly clustering the outflows. Figure 6 therefore only shows the map of clusters identified from the high angular resolution maps. The number of clusters is given as input parameter. We increased the number of clusters from 3 to 9 (i.e. the number of features) and identify gradually the components in the corresponding cluster maps. For three clusters (from cluster 0 to 2 in Fig. 6), the noise in black, the north outflows seen in SO and SiO, and the central "Protostars" component seen in OCS in blue are identified. For four clusters, the south outflow component is identified. For five clusters, the hot corino from 4A2 is identified in yellow. For six clusters, the north outflow is decomposed into two low-velocity ("North(LV)" in cyan) and high-velocity ("North(HV)" in salmon) components. For seven clusters, the south outflow is decomposed into a SiO-only emission ("South(SiO)" in orange) and SO+SiO emission ("South(SO+SiO)" in green). For eight clusters, the OCS peak (in purple) is identified. For nine clusters,

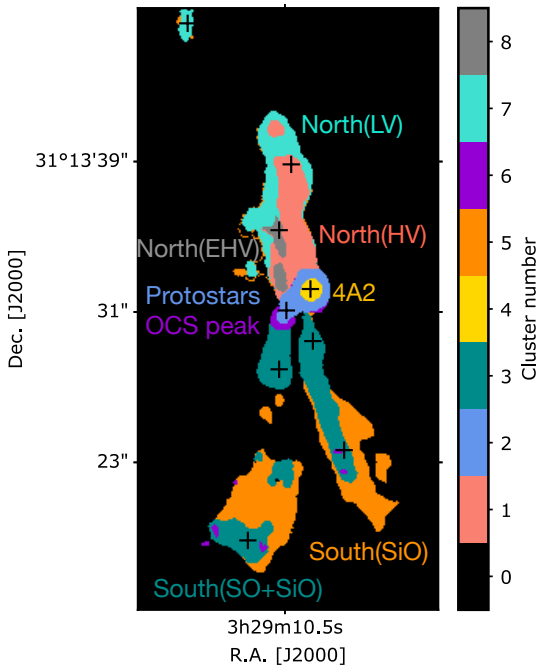


Fig. 6. Map of the clusters estimated by the K-Means algorithm based on the moment 0, 1, and 2 maps of the SiO(5−4), SO(4_5−3_4), and OCS(17−16) molecular emissions (see text for more details).

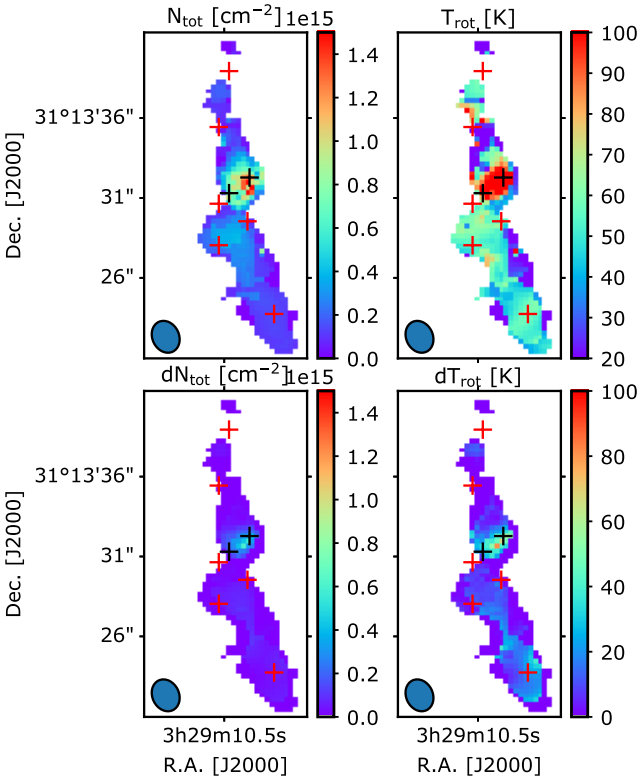


Fig. 7. Column density $N_{\rm tot}$ and rotational temperature $T_{\rm rot}$ and maps (*top panels*) together with their uncertainties d$N_{\rm tot}$ and d$T_{\rm rot}$ (*bottom panels*) obtained from a rotational diagram analysis when the flux of at least three SO_2 transitions is higher than four times the σ rms noise level of each map.

the extremely-high-velocity component ("North(EHV)" in grey) is clearly identified, as already shown by the moments 1 and 2 in Fig. 4.

We also estimated the effect of noise on the clustering results by adding a random Gaussian noise to the moment 0 maps with standard deviations equal to those listed in Table 1. Adding a random noise to our dataset gives very similar results. All clusters but the North(EHV) are identified, whilst cluster 0 depicting the noise in black is decomposed into two randomly spatially distributed clusters.

This simple clustering method therefore allows us to quantitatively dissect the outflows into several components that were already qualitatively suspected by eye. More sophisticated clustering methods have been proven to be efficient to dissect larger and more complex regions where a visual inspection is impossible (see Bron et al. 2018, for instance).

4. Radiative transfer analysis

4.1. Rotational diagram analysis

The moment maps from the SO_2 transitions at ∼143 and ∼165 GHz share similar observational properties (similar frequency, angular resolution, configuration of the interferometer array, and rms noise). Their detection therefore allows us to self consistently analyse their emission and therefore to investigate the evolution of the physical conditions along the outflows driven by IRAS4A. We start with a Rotational Diagram (RD) analysis to estimate the SO_2 column density and the rotational temperature throughout the outflows (Goldsmith & Langer 1999). For this purpose, we extracted the flux of each pixel, set to 0.3 arcsec, of the velocity-integrated blue-shifted (−10; +7 km s^{-1}) and red-shifted (+7; +20 km s^{-1}) interferometric maps for the four SO_2 transitions at ∼143 and ∼165 GHz with Einstein coefficients higher than 10^{-5} s^{-1}, spanning a range of upper level energies between 23 and 137 K. The RD analysis is performed assuming LTE and optically thin emission when at least three SO_2 transitions show a flux higher than 4σ, σ being the noise level in each moment 0 map listed in Table 1.

Figure 7 shows the SO_2 rotational temperature and column density maps together with their uncertainties derived from the RD analysis. The SO_2 column density is about $3-5 \times 10^{14}$ cm^{-2} along the outflow driven by 4A2 and increases up to 1.4×10^{15} cm^{-2} near source 4A2. The rotational temperature of SO_2 remains close to 50−60 K throughout the outflow and increases up to ∼100 K in the hot corino of IRAS4A2. In order to assess whether the lower SO_2 rotational temperature derived in the outflow with respect to the hot corino could be due to sub-thermal excitation of the levels, given the high critical densities of its transitions ($1-3 \times 10^6$ cm^{-3}), or to lower kinetic temperatures, a non-LTE analysis taking the collisional and radiative processes into account is needed.

For other species, the low number of transitions and their similar upper level energies prevent us to carry out a full rotational diagram analysis. Following the opacity estimates carried out in Sect. 3.2, we estimated the column density ratios along the outflows using the OCS(8−7), $C^{34}S(2-1)$, SO(3_2−2_1), and $SO_2(8_{1,7}-8_{0,8})$ transitions that have close upper level energies between 7 and 37 K. We assumed a rotational temperature $T_{\rm rot}$ = 50 K following the SO_2 rotational diagram analysis and optically thin emission.

Figure 8 presents the column density ratio maps between OCS, SO_2, SO, and CS. As expected from the intensity maps, the OCS/SO_2 abundance ratio increases from ∼1 in the SW outflow driven by 4A2 to ∼4 in the south outflow driven by

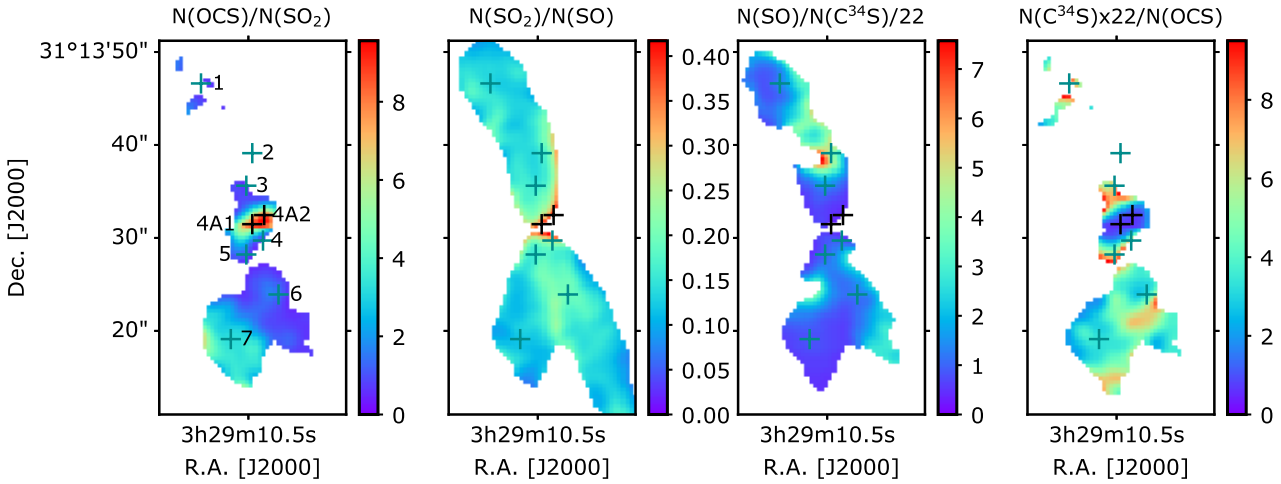


Fig. 8. Column density ratio maps betweeen OCS, SO_2, SO, and CS obtained from a rotational diagram analysis when the flux of of both transitions are higher than six times the σ rms noise level.

Table 3. Best-fit models and 1σ uncertainties of the non-LTE RADEX analysis of SO_2 emission towards several SiO peaks.

Peak	Coordinates		Best-fit properties			T_{ex} (K)			
	RA Offset	Dec Offset	n_{H2} (cm^{-3})	T_{kin} (K)	N_{tot} (cm^{-2})	165.144 (GHz)	165.225 (GHz)	163.605 (GHz)	143.057 (GHz)
SiO 2 (4A2 outflow: N)	−0.1	7.5	$8^{+12}_{-5} \times 10^5$	95^{+40}_{-30}	$2.5 \pm 0.5 \times 10^{14}$	26	204	33	11
SiO 3 (4A2 outflow: N)	0.5	4.1	$1.2^{+5.0}_{-0.8} \times 10^6$	70^{+50}_{-20}	$2.5 \pm 1.0 \times 10^{14}$	38	115	39	–
SiO 4 (4A2 outflow, SW)	−1.3	−1.8	$3.2^{+4.0}_{-1.0} \times 10^5$	325^{+225}_{-75}	$1.5 \pm 0.5 \times 10^{14}$	24	−112	26	9
SiO 5 (4A1 outflow, SE)	0.5	−3.2	$1.2^{+3.0}_{-0.5} \times 10^6$	70^{+30}_{-10}	$2.5 \pm 0.5 \times 10^{14}$	38	115	39	14
SiO 6 (4A2 outflow, SW)	−2.9	−7.5	$1.8^{+4.0}_{-1.0} \times 10^5$	200^{+250}_{-80}	$1.3 \pm 0.5 \times 10^{14}$	10	48	20	–

4A1. The SO_2/SO abundance ratio slightly decreases from 0.2 to 0.1 between the SW outflow and the south outflow. One can notice that the SO abundance is remarkably high with respect to CS towards SiO peak 2, with a SO/CS abundance ratio of 7, whilst it remains close to 1 throughout the outflows. Column density ratio errors induced by the flux calibration uncertainties are about 30%.

4.2. Non-LTE RADEX analysis

A non-LTE analysis of the SO_2 emission, the only molecule studied in this work with at least four detected transitions with similar observational properties, is performed by using the non-LTE radiative transfer code RADEX (van der Tak et al. 2007). To this mean, we assumed an isothermal and homogeneous medium without large-scale velocity fields, a comparable method to the Large Velocity Gradient (LVG) analysis. We used the collision rate coefficients of SO_2 with H_2 computed by Balança et al. (2016) within the infinite order sudden (IOS) approximation in the 100–1000 K temperature range. The line excitation temperatures T_{ex}, the opacities τ, and the integrated brightness temperatures T_{mb} were computed by varying the SO_2 column density between 10^{13} and 10^{15} cm^{-2}, the H_2 density between 10^4 and 10^8 cm^{-3}, and the kinetic temperature T_{kin} between 50 and 550 K. We assumed a FWHM linewidth of 6 and 3 km s^{-1} for the blue- and red-shifted emissions, respectively. The analysis was performed towards the SiO peaks where at least three of the 165.144, 165.225, 163.605, and 143.057 GHz SO_2 transitions, observed with similar observational properties, are detected at a 3σ level. Best-fit properties together with their 1σ uncertainties for the physical conditions and the excitation temperatures are given in Table 3.

For the SiO peaks where the RADEX analysis has been performed, the SO_2 emission is reproduced for densities between 10^5 and 10^6 cm^{-3}. These best-fit densities are lower than the critical densities of all SO_2 transitions ($\sim 3 \times 10^6$ cm^{-3} for the transitions at 163–165 GHz and 1×10^6 cm^{-3} at 143.057 GHz). The three SiO peaks where the best-fit density is about 10^6 cm^{-3} show best-fit temperatures lower than 100 K whilst the two SiO peaks with a lower best-fit density of $2–3 \times 10^5$ cm^{-3} show best-fit temperatures higher than 200 K. The different physical conditions inferred from the RADEX analysis could be due to different physical shock conditions or emitting SO_2 positions within shocks. But given the best-fit densities found here, it is possible that SO_2 traces the already compressed thermalisation zone or the post-shock region where densities are higher.

All transitions but the one at 165.225 GHz show low excitation temperatures between 10 and 40 K. In contrast, the excitation temperature of the transition at 165.225 GHz is higher than the kinetic temperature towards SiO peaks 2, 3, and 5 whilst it is negative towards SiO peak 4. This suggests that this transition could be masering, explaining its brighter emission with respect to others with similar spectroscopic properties.

Column densities derived with the non-LTE analysis are about $1.3–2.5 \times 10^{14}$ cm^{-2} and are very similar to those derived with the RD analysis. They therefore suggest that the RD analysis

gives a good estimate of the SO_2 column density throughout the outflow. For the best-fit properties, SO_2 transitions are optically thin with opacities lower than 0.1.

5. Comparison with astrochemical predictions

5.1. The modelling

In this section, we aim to interpret the chemical evolution of sulfuretted species observed along the outflows driven by the NGC 1333-IRAS4A protobinary system thanks to theoretical predictions of chemical abundances through the passage of shocks.

Given the lack of secured detections of sulfuretted species in ices, the pre-shock abundances of sulfuretted species in interstellar ices are highly uncertain. Palumbo et al. (1997) searched for the absorption feature at 4.90 μm attributed to OCS towards a sample of massive protostars, resulting in a detection towards three sources with associated solid OCS abundances of $2.3-7.0 \times 10^{-8}$ relative to the number of H nuclei. However, upper limits of the OCS abundance down to 3.8×10^{-9} have also been derived. Smith et al. (1991) searched for the absorption band at 3.90 μm attributed to H_2S towards six protostars, resulting in non-detections only. The derived upper limits of solid H_2S abundances between $<4 \times 10^{-8}$ and $<1.6 \times 10^{-7}$ are slightly lower but not inconsistent with the atomic sulfur abundance of $1-4 \times 10^{-7}$ estimated by Anderson et al. (2013) towards IRAS4A. According to Boogert et al. (2015), solid SO_2 has been possibly identified towards only one line of sight so far through a relatively good fit of the absorption band observed at 7.58 μm with a SO_2:CH_3OH mixture resulting in an absolute abundance of $\sim 4 \times 10^{-7}$ (Boogert et al. 1997).

Here, we decide to adopt a two-stage approach. In the first stage, the cold gas-grain chemistry is followed for constant dark cloud physical conditions with the MOMICE gas-grain astrochemical model modified and updated from the GRAINOBLE model (Taquet et al. 2012, 2013, 2014, 2016; Dulieu et al. 2019) in order to estimate the pre-shock abundances. In the second stage, the physical-chemical evolution impacted by stationary one-dimensional Continuous (C) magnetised shocks is followed using the 2015 version of the Paris-Durham shock model (Flower & Pineau des Forêts 2015). The dynamical age of the IRAS4A outflows is likely of a few 10^4 yr, which should be much longer than the equilibrium time of 1000–2000 yr for the shock waves considered in this work, justifying the choice of stationary C-type shocks.

The gas phase chemical network used in MOMICE for the first stage is based on the 2013 version of the KIDA database updated for reactions involving sulfuretted species following Smith et al. (2004), Loison et al. (2012), and Vidal et al. (2018). The surface chemical network is based on that of Taquet et al. (2016) and is updated following recent works focusing on sulfur chemistry in ices (Vidal et al. 2018; Laas & Caselli 2019). The initial elemental abundances are taken from the "low-metal abundances" set EA1 of Wakelam & Herbst (2008) whilst we set the initial abundance of S^+ to 4×10^{-7}, corresponding to the maximum atomic sulfur abundance derived by Anderson et al. (2013) from S[I] observations towards IRAS4A with *Spitzer*. The initial abundances are the following: $X(H_2) = 0.5$; $X(He) = 9.00 \times 10^{-2}$; $X(C^+) = 7.3 \times 10^{-5}$; $X(O) = 1.76 \times 10^{-4}$; $X(N) = 2.14 \times 10^{-5}$; $X(Si) = 8.0 \times 10^{-9}$; $X(Na) = 2.0 \times 10^{-9}$; $X(Mg) = 7.0 \times 10^{-9}$; $X(S^+) = 4.2 \times 10^{-7}$; $X(Fe^+) = 3.00 \times 10^{-9}$. The chemistry is followed for typical molecular cloud physical conditions: a constant density $n_H = 2 \times 10^4$ cm^{-3}, a visual extinction $A_V = 20$ mag, a cosmic ray ionisation rate $\zeta = 1.0 \times 10^{-17}$ s^{-1}, and for two constant temperatures $T_{gas} = T_{dust} = 10$ and 20 K until the time reaches 10^6 yr (i.e. ~3 times the free-fall time at $n_H = 2 \times 10^4$ cm^{-3}).

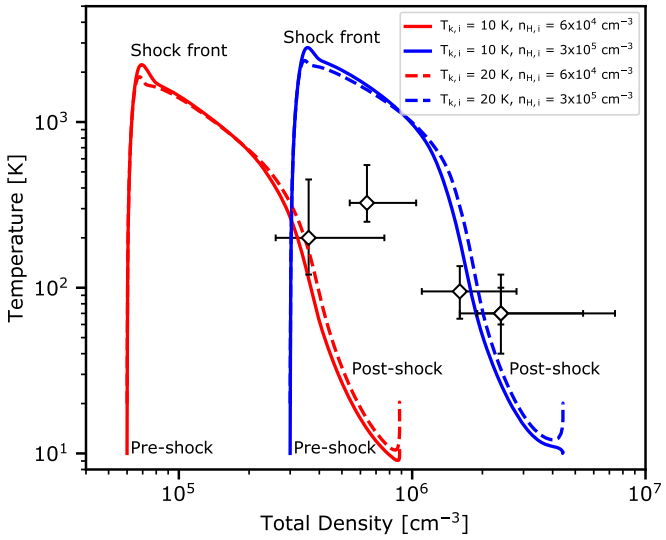


Fig. 9. Comparison between the density and temperature evolutions as predicted by the Paris-Durham shock model (coloured curves) for initial pre-shock densities of 6×10^4 and 3×10^5 cm^{-3} and initial temperatures of 10 and 20 K with the densities and temperatures estimated with the RADEX analysis of the SO_2 emission towards various SiO peaks (diamonds; see Table 3).

In the second stage, we consider C-shocks with a shock velocity of 20 km s^{-1} and pre-shock (dust and gas) temperatures of 10 and 20 K. To choose the pre-shock densities, we first compared the evolution of density and gas temperature as predicted by the Paris-Durham shock model for various pre-shock densities $n_{H,ini}$ with those found with the RADEX analysis of the SO_2 emission presented in Sect. 4.2. As shown in Fig. 9, it is found that shocks with $n_{H,ini}$ between 6×10^4 and 3×10^5 cm^{-3} reproduce the different observed density and temperature values in the post-shock zones where the gas cools down through radiative cooling. We therefore used these two pre-shock density values for the modelling. The chemical network used in the shock code is based on that of Flower & Pineau des Forêts (2015) updated for sulfur chemistry following Smith et al. (2004), Loison et al. (2012), and Vidal et al. (2018). In total, the network includes 144 gaseous, icy, or refractory species linked by 1070 chemical processes, and contains only the following sulfuretted species: S, HS, H_2S, CS, SO, SO_2, OCS, S^+, HS^+, H_2S^+, H_3S^+, CS^+, HCS^+, SO^+, HSO^+, HSO_2^+, and $HOCS^+$. This network is consequently smaller than the one used in the first stage, but includes the most important formation and destruction reactions for H_2S, OCS, CS, SO, and SO_2 and for the oxygenated species O, OH, O_2, and H_2O, that are key for the sulfur chemistry.

5.2. Results

The left panels of Fig. 10 show the temporal evolution of the absolute abundances of the main sulfuretted species in ices and in the gas phase predicted by the MOMICE astrochemical model at $n_H = 2 \times 10^4$ cm^{-3}, $T = 10$ and 20 K, $\zeta = 10^{-17}$ s^{-1}, and $A_V = 20$ mag. H_2S is the one of the most abundant sulfuretted molecules in ices with a final abundance of $\sim 2 \times 10^{-7}$ and $\sim 1 \times 10^{-7}$ at 10 and 20 K, respectively. These values are similar to

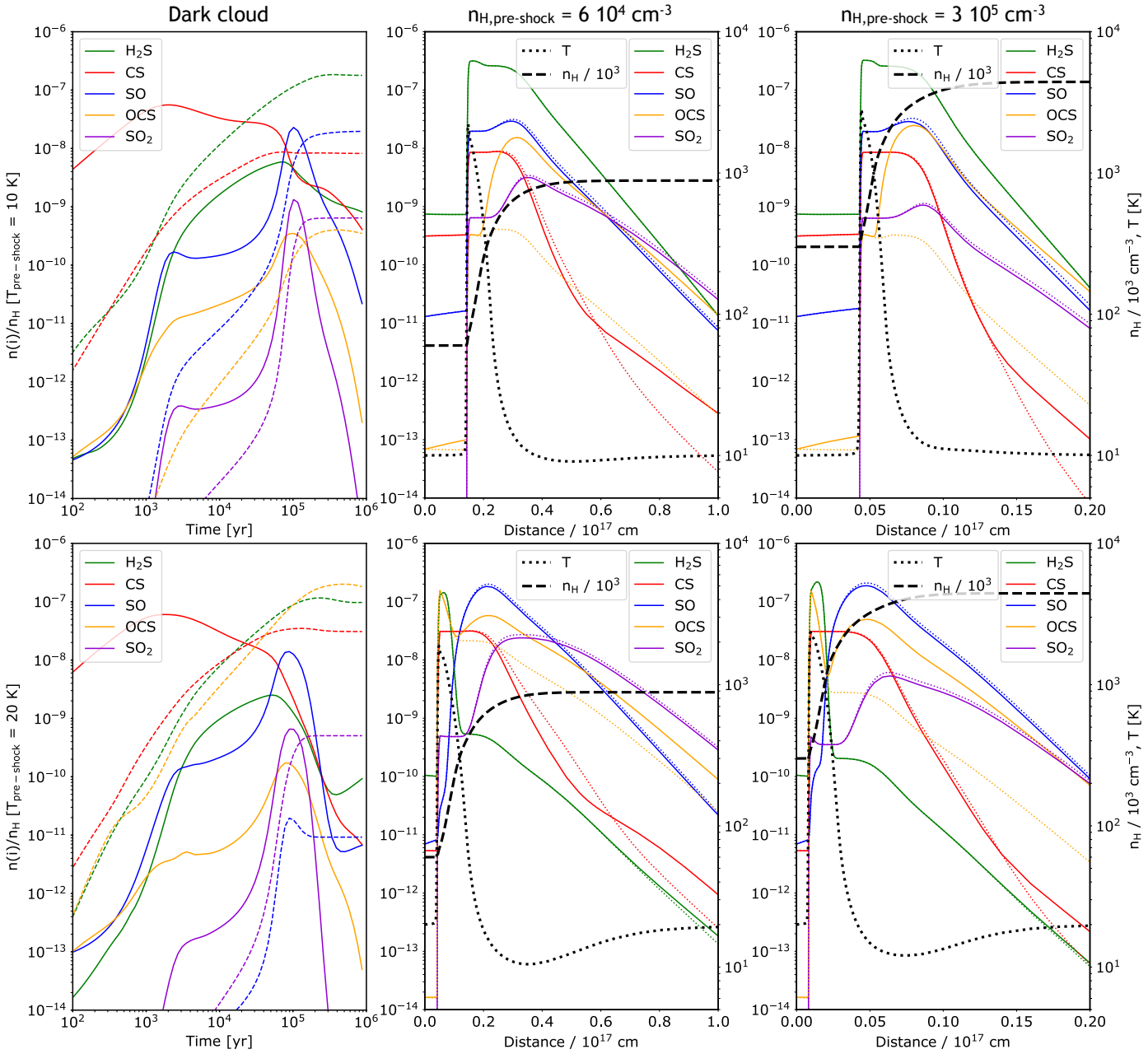


Fig. 10. *Left panels*: absolute abundances of selected sulfuretted species as a function of time predicted by the GRAINOBLE astrochemical model in the gas phase (solid curves) and in interstellar ices (dashed curves) at 10 K (*top*) and 20 K (*bottom*) and for $n_{\rm H} = 2 \times 10^4$ cm^{-3}, $\zeta = 10^{-17}$ s^{-1}, and $A_{\rm V} = 20$ mag. *Middle and right panels*: gaseous absolute abundances of selected sulfuretted species (coloured curves) and physical conditions (black curves) profiles in 1D C-type shocks predicted by the Paris-Durham shock code for a pre-shock density of 6×10^4 cm^{-3} (*centre panels*) and 3×10^5 cm^{-3} (*right panels*). Solid and dashed coloured curves show the abundances with and without the OCS formation/destruction reactions introduced by Loison et al. (2012), respectively (see text for more details). For the shocks considered here, the entire icy material formed in dark clouds is sputtered in the shock front, final ice abundances in the left panels are therefore similar to the gas phase obtained at the shock front in the *middle and right panels*, with the exception of H_2S that is efficiently formed through hot gas phase chemistry.

the observed upper limits in abundances derived by Smith et al. (1991). The surface chemistry of H_2S is thought to be similar to that of water, atomic sulfur is efficiently hydrogenated through addition reactions involving H atoms through HS, assumed to be barrierless. The abundance of solid SO dramatically decreases from 10^{-8} to 2×10^{-11} between 10 and 20 K because of the increasing diffusion of carbon atoms along the surface that increases the reactivity of the SO+C reaction forming CO+S. On the other hand, the abundance of solid OCS increases strongly with the temperature, from 4×10^{-10} to 2×10^{-7}, between 10 and 20 K. Like CO_2, solid OCS formation is triggered for moderate temperatures of 15–20 K since the relatively heavy species S, CO and CS start to diffuse along the surface and react with radicals such as OH and HS to form OCS. CS is the third most abundant molecule in ices with an abundance of $1{-}3 \times 10^{-8}$. Unlike H_2S, most solid CS has a gas phase origin and is then efficiently trapped "intact" in ices after its freeze-out. Indeed, its most important destruction reaction on ices, converting solid CS to solid HCS, has a limited efficiency because it is thought to have an activation barrier of ~1000 K (see Vidal et al. 2018).

The abundance of SO_2 is about 10^{-9} between 10 and 20 K and is mostly due to gas phase chemistry followed by freeze-out. The predicted abundance is two orders of magnitude lower than the solid SO_2 abundance derived by Boogert et al. (1997) towards the massive protostar W33A. However, according to Boogert et al. (2015) SO_2 has only possibly been identified so far, and more secured detections are needed to confirm the presence of SO_2 in ices.

The final abundances predicted by MOMICE are considered as initial pre-shock abundances in the shock code. The centre and right panels of Fig. 10 show the spatial evolution of the gas phase abundances of the sulfuretted species within shocks for pre-shock densities $n_{\rm H,ini}$ of 6×10^4 and 3×10^5 cm^{-3}, pre-shock temperatures of 10 and 20 K, and a shock velocity of 20 km s^{-1}. The compression of the material at the shock front induces an increase of the total density and a sudden increase of the gas temperature between 2000 and 3000 K, the exact value depending on the shock velocity, the initial density, and the pre-shock temperature. The dust temperature is assumed to remain constant over time, and remains equal to the initial temperature of 10 or 20 K. Behind the shock front, radiative cooling efficiently decreases the temperature of the gas down to its initial temperature. The electronic abundance at $T_{\rm pre-shock}$ = 20 K predicted by MOMICE is higher than at 10 K by a factor of two, increasing the coupling between the neutral and ionised gas, and inducing a faster compression of the gas.

For the shock velocity of 20 km s^{-1} considered here, the entire icy material is sputtered into the gas phase within the shock front. However, the refractory material remains intact after the passage of such shocks since refractory grains start to be efficiently destroyed through sputtering for shocks faster than typical 30–40 km s^{-1} (see May et al. 2000). Once sputtered, H_2S and OCS can be efficiently destroyed in the gas through the H_2S+H and OCS+H abstraction reactions since they have moderate activation barriers of 860 and 2000 K, respectively (Schofield 1973; Tsunashima et al. 1975). Such barriers can be overcome at temperatures higher than 1000 K reached in the shock front for about 30–80 yr, depending on the pre-shock density. An initial temperature of 20 K increases the pre-shock abundance of atomic H in the gas phase by about two orders of magnitude because H atoms cannot deplete efficiently on grains, increasing the efficiency of these destruction reactions of H_2S and OCS. Reactions between atomic H and SO or SO_2, on the other hand, have activation barriers higher than 10 000 K (Leen & Graff 1988; Blitz et al. 2006). SO and SO_2 can therefore survive during their passage in the shock front for the shocks considered here.

Behind the shock front, the abundance of SO increases with the distance from the shock, especially for the models considering an initial temperature of 20 K where SO has a low initial abundance. SO_2 is then formed later on at larger distances with respect to the shock front. SO is mainly formed through three barrierless neutral-neutral S+OH, HS+O, and S+O_2 reactions in the warm gas. All species involved in SO formation have moderately high abundances, between 10^{-9} and 5×10^{-7}, after the shock front, and allow for an efficient formation of SO. SO is then gradually converted into SO_2 mainly through the SO+OH barrierless reaction. SO_2 reaches its maximal abundance behind the shock at a distance of $3-4 \times 10^{16}$ and $6-8 \times 10^{15}$ cm for pre-shock densities of 6×10^4 and 3×10^5 cm^{-3}, respectively. Unlike SO and SO_2, H_2S cannot be efficiently formed in the gas phase behind the shock and its abundance gradually decreases due to freeze-out onto dust grains.

For OCS, the situation is more complex. Loison et al. (2012) recently introduced a few reactions that are potentially important for OCS formation and destruction, notably the CS+OH, SO+CH, S+HCO, OCS+CH, and OCS+C reactions. The CS+OH was already present in astrochemical networks but with a low rate ($\alpha = 9.4 \times 10^{-14}$ cm^{-3} s^{-1}; γ = 800 K; Leen & Graff 1988) whilst the SO+CH and S+HCO reactions were not present in astrochemical networks, Loison et al. (2012) estimated them to be reactive with rates of $\sim 1 \times 10^{-10}$ cm^{-3} s^{-1}. Dotted coloured lines in the centre and right panels of Fig. 10 show the chemical abundances without the new reactions introduced by Loison et al. (2012). It can be seen that, without these new reactions, OCS is not efficiently formed in the post-shock gas phase and OCS would be mostly present in the shock front, similar to H_2S (as recently suggested by Podio et al. 2014; Holdship et al. 2016), especially at $T_{\rm pre-shock}$ = 20 K when the OCS abundance is high. On the other hand, the incorporation of the reactions suggested by Loison et al. (2012) triggers the formation of gaseous OCS behind the shock and OCS behaves like SO. For a pre-shock temperature of 20 K, the OCS abundance first drops because of "hot" gas-phase chemistry before re-increasing due to the barrierless CS+OH and SO+CH reactions. After its sputtering in the shock front, CS is not significantly affected by hot nor warm gas phase chemistry, its abundance remains constant near the shock before decreasing due to freeze-out onto dust grains.

The gradual transition between H_2S, OCS, SO, and SO_2 shown here confirms the earlier predictions by Pineau des Forets et al. (1993) in shocks and by Charnley (1997) and Wakelam et al. (2004) in hot cores. The main differences with respect to the work Pineau des Forets et al. (1993) is the incorporation of OCS in the chemical network and the H_2S formation in cold interstellar ices subsequently sputtered in the shock front in our work whilst Pineau des Forets et al. (1993) formed H_2S in the shock front from ion-neutral reactions through SH^+ and H_2S^+.

In conclusion, the modelling presented here suggests that H_2S should trace the shock front where the icy material has been recently sputtered whilst SO_2 would rather trace the post-shock regions. This would explain why SO_2 is mostly detected towards the NE-SW outflow driven by IRAS4A2 since this outflow is much more elongated and consequently likely older. SO and CS should be abundant both in the shock front and behind the shock regardless of the shock velocities, explaining their bright and extended emission throughout the two outflows. However, the evolution of the SO/CS column density ratio along the outflows, especially near SiO peak 2, could be explained by a different chemical behaviour behind shocks, SO being formed at moderate gas phase temperatures unlike CS.

With the new reactions introduced by Loison et al. (2012), the OCS abundance profiles along the shocks are complex and mostly depend on the initial pre-shock temperature that governs the OCS abundance in ices. Our observations show that OCS is much brighter in the shorter, and likely younger, south outflow driven by IRAS4A1 similarly to CH_3OH as seen in Fig. 1. These observations would agree well with the models considering a pre-shock temperature of ~20 K, where OCS is mostly abundant in shock fronts and the OCS maps do not show any evidence for efficient gas phase formation behind shocks through the reactions suggested by Loison et al. (2012) since we do not observe any enhanced emission on larger scales, like SO for instance.

The conclusions given by the present modelling strongly rely on the predicted abundances of sulfuretted species locked in interstellar ices, which are still poorly constrained by observations. New infrared observations of interstellar ices will soon be carried out with the *James Webb* Space Telescope at high sensitivity and spectral resolution, likely resulting in more robust estimates of the sulfur reservoir in ices. Observing H_2S towards the

IRAS4A system at a similar angular resolution would also help us to disentangle the puzzling chemistry of OCS in outflows.

6. Conclusions

This work presents multi-line interferometric observations of various sulfuretted species towards the outflows driven by the NGC 1333-IRAS4A protobinary system with the IRAM-NOEMA interferometer. We analysed the spatial and kinematical evolutions along the outflows of the emission from various OCS, CS, SO, and SO_2 transitions detected at different frequencies in the 1.3, 2, and 3 mm bands for two typical angular resolutions of 1 and 2–4″. We used clustering methods and radiative models to evaluate the evolution of the physical and chemical conditions. We also used the state-of-the-art one-dimensional Paris-Durham shock model to study the sulfur chemistry in shocks with the goal of interpreting the chemical differentiation observed along the outflows. We summarise here the main results of our work:

– OCS, CS, SO, SO_2 clearly show different spatial emission along the two outflows driven by IRAS4A. Integrated emission maps reveal that OCS is brighter in the south outflow driven by IRAS4A1 whereas SO_2 is rather detected along the outflow driven by IRAS4A2 extended along the north east–south west (NE–SW) direction. CS and SO show extended emission along the two outflows.

– SO is detected at extremely-high velocity up to +25 km s^{-1} relative to the source velocity, clearly allowing us to distinguish the outflow driven by IRAS4A1 along the north–south direction from the NE–SW outflow driven 4A2. Other sulfuretted species are mostly detected at lower velocities. OCS in particular shows an intriguing "blue" low velocity (<5 km s^{-1} relative to source velocity) emission peak at the beginning of the south outflow traced by SiO and SO.

– Column density ratio maps have been estimated from a rotational diagram analysis and allowed us to confirm a clear gradient of the OCS/SO_2 column density ratio between the outflow driven by IRAS4A1 and the one triggered by 4A2.

– Non-LTE analysis of four SO_2 transitions towards several SiO emission peaks suggests that associated gas should be relatively dense, with densities higher than 10^5 cm^{-1}, and relatively warm ($T > 100$ K) temperatures in most cases.

– A comparison with theoretical predictions carried out with the state-of-the-art Paris-Durham shock model allowed us to give an interpretation of the chemical evolution of sulfur chemistry along the two outflows, in spite of the complex chemistry at work. OCS would have been efficiently formed in "warm" interstellar ices, namely at $T \sim 20$ K, and then recently released in the gas phase of shock through sputtering processes, explaining its bright emission in the likely young south outflow driven by IRAS4A1. In contrast, SO_2 should be rather formed behind the shock front through warm gas phase chemistry, explaining why SO_2 is mostly detected towards the more elongated and likely older NE–SW outflow driven by IRAS4A2. SO and CS should be abundant both in the shock front and behind the shock regardless of the shock conditions, explaining their bright and extended emission throughout the two outflows.

Acknowledgements. V.T. is grateful to Sylvie Cabrit and Guillaume Pineau des Forêts for stimulating discussions on the chemistry in shocks. The authors acknowledge the CALYPSO consortium for the use of the CALYPSO dataset. This work is based on observations carried out with the IRAM PdBI/NOEMA Interferometer under project numbers V05B and V010 (PI: M.V. Persson), U003 (PI: V. Taquet), and L15AA (PI: C. Ceccarelli and P. Caselli). IRAM is supported by INSU/CNRS (France), MPG (Germany) and IGN (Spain). V.T. acknowledges the financial support from the European Union's Horizon 2020 research and innovation programme under the Marie Sklodowska-Curie grant agreement n. 664931. This work was supported by (i) the PRIN-INAF 2016 "The Cradle of Life – GENESIS-SKA (General Conditions in Early Planetary Systems for the rise of life with SKA)", (ii) the European Research Council (ERC) under the European Union's Horizon 2020 research and innovation programme, for the Project "The Dawn of Organic Chemistry" (DOC), grant agreement No 741002, and (iii) the European MARIE SKŁODOWSKA-CURIE ACTIONS under the European Union's Horizon 2020 research and innovation programme, for the Project "Astro-Chemistry Origins" (ACO), Grant No 811312. C.F. acknowledges support from the French National Research Agency in the framework of the Investissements d'Avenir program (ANR-15- IDEX-02), through the funding of the "Origin of Life" project of the Université Grenoble-Alpes.

References

Anderson, D. E., Bergin, E. A., Maret, S., & Wakelam, V. 2013, ApJ, 779, 141
André, P., Men'shchikov, A., Bontemps, S., et al. 2010, A&A, 518, L102
Bachiller, R., Liechti, S., Walmsley, C. M., & Colomer, F. 1995a, A&A, 295, L51
Bachiller, R., Codella, C., Colomer, F., et al. 1995b, A&A, 335, 266
Bachiller, R., Pérez Gutiérrez, M., Kumar, M. S. N., et al. 2001, A&A, 372, 899
Balança, C., Spielfiedel, A., & Feautrier, N. 2016, MNRAS, 460, 3766
Benedettini, M., Viti, S., Codella, C., et al. 2007, MNRAS, 381, 1127
Benedettini, M., Viti, S., Codella, C., et al. 2013, MNRAS, 436, 179
Blitz, M.A., Hughes, K.J., Pilling, M.J., & Robertson, S.H. 2006, J. Phys. Chem. A, 110, 2996
Boogert, A. C. A., Schutte, W. A., Helmich, F. P., Tielens, A. G. G. M., & Wooden, D. H. 1997, A&A, 317, 929
Boogert, A. C. A., Gerakines, P. A., & Whittet, D. C. B. 2015, ARA&A, 53, 541
Bottinelli, S., Ceccarelli, C., Lefloch, B., et al. 2004, ApJ, 615, 354
Bottinelli, S., Ceccarelli, C., Williams, J. P., & Lefloch, B. 2007, A&A, 463, 601
Bron, E., Daudon, C., Pety, J., et al. 2018, A&A, 610, A12
Bruderer, S., Benz, A. O., Doty, S. D., et al. 2009, ApJ, 700, 872
Busquet, G., Lefloch, B., Benedettini, M., et al. 2014, A&A, 561, A120
Caselli, P., Hartquist, T. W., & Havnes, O. 1997, A&A, 322, 296
Ceccarelli, C., Caselli, P., Fontani, F., et al. 2017, ApJ, 850, 176
Charnley, S. B. 1997, ApJ, 481, 396
Ching, T.-C., Lai, S.-P., Zhang, Q., et al. 2016, ApJ, 819, 159
Choi, M. 2005, ApJ, 630, 976
Choi, M., Tatematsu, K., Park, G. & Kang, M. 2007, ApJ, 667, L183
Choi, M., Kang, M., Tatematsu, K., et al. 2011, PASJ, 63, 1281
Codella, C., & Bachiller, R. 1999, A&A, 350, 659
Codella, C., Bachiller, R., Benedettini, M., et al. 2005, MNRAS, 361, 244
Codella, C., Benedettini, M., Beltrán, M. T., et al. 2009, A&A, 507, L25
Codella, C., Lefloch, B., Ceccarelli, C., et al. 2010, A&A, 518, L112
Codella, C., Ceccarelli, C., Caselli, P., et al. 2017, A&A, 605, L3
David, A., & Vassilvitskii, S. 2007, Proceedings of the eighteenth annual ACM-SIAM symposium on Discrete algorithms, Society for Industrial and Applied Mathematics
De Simone, M., Codella, C., Ceccarelli, C., et al. 2019, A&A, submitted
Draine, B. T., & Salpeter, E. E. 1979, ApJ, 231, 438
Dulieu, F., Nguyen, T., Congiu, E., Baouche, S., & Taquet, V. 2019, MNRAS, 484, L119
Flower, D. R., & Pineau des Forets, G. 1994, MNRAS, 268, 724
Flower, D. R., & Pineau Des Forêts G. 2003, MNRAS, 343, 390
Flower, D. R., Pineau Des Forêts, G., & Rabli, D. 2010, MNRAS, 409, 29
Flower, D. R., & Pineau des Forêts, G. 2015, A&A, 578, A63
Geppert, W. D., Hamberg, M., Thomas, R. D., et al. 2006, Faraday Discuss., 133, 177
Goldsmith, P. F., & Langer, W. D. 1999, ApJ, 517, 209
Gómez-Ruiz, A. I., Codella, C., Lefloch, B., et al. 2015, MNRAS, 446, 3346
Green, S. 1995, ApJS, 100, 213
Gueth, F., Guilloteau, S., & Bachiller, R. 1998, A&A, 333, 287
Guillet, V., Pineau Des Forêts, G., & Jones, A. P. 2007, A&A, 476, 263
Gusdorf, A., Cabrit, S., Flower, D. R., et al. 2008a, A&A, 482, 809
Gusdorf, A., Pineau Des Forêts, G., Cabrit, S., et al. 2008b, A&A, 490, 695
Hasegawa, T. I., & Herbst, E. 1993, MNRAS, 263, 589
Herbst, E., & van Dishoeck, E. F. 2009, ARA&A, 47, 427
Hirota, T., Bushimata, T., Choi, Y. K., et al. 2008, PASJ, 60, 37
Holdship, J., Viti, S., Jimenez-Serra, I., et al. 2016, MNRAS, 463, 802
Holdship, J., Jimenez-Serra, I., Viti, S., et al. 2019, ApJ, 878, 64
Kristensen, L. E., van Dishoeck, E. F., Bergin, E. A., et al. 2012, A&A, 542, A8
Ladjelate, B., André, P., Könyves, V., et al. 2020, A&A, in press https://doi.org/10.1051/0004-6361/201936442
Laas, J. C., & Caselli, P. 2019, A&A, 624, A108
Leen, T. M., & Graff, M. M. 1988, ApJ, 325, 411
Lefèvre, C., Cabrit, S., Maury, A. J., et al. 2017, A&A, 604, L1

Lefloch, B., Ceccarelli, C., Codella, C., et al. 2017, MNRAS, 469, L73
Lefloch, B., Bachiller, R., Ceccarelli, C., et al. 2018 MNRAS, 477, 4792
Lloyd, S. 1982, IEEE Trans. Inf. Theory, 28, 2
Loison, J.-C., Halvick, P., Bergeat, A., Hickson, K. M., & Wakelam, V. 2012, MNRAS, 421, 1476
Looney, L. W., Mundy, L. G., & Welch, W. J. 2000, ApJ, 529, 477
López-Sepulcre, A., Sakai, N., Neri, R., et al. 2017, A&A, 606, A121
Maury, A. J., André, P., Testi, L., et al. 2019, A&A, 621, A76
May, P. W., Pineau des Forêts, G., Flower, D. R., et al. 2000, MNRAS, 318, 809
Nisini, B., Benedettini, M., Codella, C., et al. 2010, A&A, 518, L120
Öberg, K. I., Boogert, A. C. A., Pontopiddan, K. M., et al. 2011, ApJ, 740, 109
Ospina-Zamudio, J., Lefloch, B., Ceccarelli, C., et al. 2018, A&A, 618, A145
Palumbo, M. E., Geballe, T. R., & Tielens, A. G. G. M. 1997, ApJ, 479, 839
Persson, M. V., Jørgensen, J. K., & van Dishoeck, E. F. 2012, A&A, 541, A39
Persson, M. V., Jørgensen, J. K., van Dishoeck, E. F., et al. 2014, A&A, 563, A74
Pineau des Forets, G., Roueff, E., Schilke, P., et al. 1993, MNRAS, 262, 915
Podio, L., Lefloch, B., Ceccarelli, C., et al. 2014, A&A, 565, A64
Pontoppidan, K. M., van Dishoeck, E. F., & Dartois, E. 2004, A&A, 426, 925
Rabli, D., & Flower, D. R. 2010, MNRAS, 406, 95
Santangelo, G., Nisini, B., Codella, C., et al. 2014, A&A, 568, A125
Santangelo, G., Codella, C., Cabrit, S., et al. 2015, A&A, 584, A126
Schofield, K. 1972, J. Phys. Chem. Ref. Data, 2, 25
Smith, R. G. 1991, MNRAS, 249, 172
Smith, I. W. M., Herbst, E., & Chang, Q. 2004, MNRAS, 350, 323
Tabone, B., Cabrit, S., Bianchi, E., et al. 2017, A&A, 607, L6
Taquet, V., Ceccarelli, C., & Kahane, C. 2012, A&A, 538, A42
Taquet, V., Peters, P. , Kahane, C., et al. 2013, A&A, 550, A127
Taquet, V., Charnley, S. B., Sipilä, O. 2014, ApJ, 791, 1
Taquet, V., López-Sepulcre, A., Ceccarelli, C., et al. 2015, ApJ, 804, 81
Taquet, V., Wirström, E., Charnley, S. B. 2016, ApJ, 821, 46
Tielens, A. G. G. M., Tokunaga, A. T., Geballe, T. R., & Baas, F. 1991, ApJ, 381, 181
Tielens, A. G. G. M., McKee, C. F., Seab, C. G., et al. 1994, ApJ, 431, 321
Tobin, J. J., Looney, L. W., Li, Z.-Y., et al. 2018, ApJ, 867, 43
Tsunashima, S., Yokota, T., Safarik, I., Gunning, H. E., & Strausz, O. P. 1975, J. Phys. Chem., 79, 775
Van der Tak, F. F. S., Black, J. H., Schöier, F. L., Jansen, D. J., & van Dishoeck, E. F. 2007, A&A 468, 627
Vidal, T. H. G., & Wakelam, V. 2018, MNRAS, 474, 5575
Viti, S., Jimenez-Serra, I., Yates, J. A., et al. 2011, ApJ, 740, L3
Visser, R., van Dishoeck, E. F., Doty, S. D., et al. 2009, A&A, 495, 881
Wakelam, V., & Herbst, E. 2008, ApJ, 680, 371
Wakelam, V., Caselli, P., Ceccarelli, C., Herbst, E., & Castets, A. 2004, A&A, 422, 159
Watanabe, N., & Kouchi, A. 2002, ApJ, 571, L173
Wilson, T. L., & Rood, R. T. 1994, ARA&A, 32, 191
Yıldız, U. A., Kristensen, L. E., van Dishoeck, E. F., et al. 2012, A&A, 542, A86
Zucker, C., Schlafly, E. F., Speagle, J. S., et al. 2018, ApJ, 869, 83

[1] INAF, Osservatorio Astrofisico di Arcetri, Largo E. Fermi 5, 50125 Firenze, Italy
e-mail: taquet@arcetri.astro.it
[2] Univ. Grenoble Alpes, CNRS, IPAG, 38000 Grenoble, France
[3] Institut de Radioastronomie Millimétrique, 38406 Saint-Martin d'Hères, France
[4] Max-Planck-Institut für Extraterrestrische Physik, Giessenbachstr. 1, 85748 Garching, Germany
[5] Laboratoire de Physique de l'ENS, ENS, Université PSL, CNRS, Sorbonne Université, Université de Paris, Paris, France
[6] Observatoire de Paris, Université PSL, Sorbonne Université, LERMA, 75014 Paris, France
[7] Department of Space, Earth, and Environment, Chalmers University of Technology, Onsala Space Observatory, 439 92 Onsala, Sweden
[8] IRAP, Université de Toulouse, CNRS, CNES, UPS, Toulouse, France
[9] Department of Physics, The University of Tokyo, 7-3-1, Hongo, Bunkyo-ku, Tokyo 113-0033, Japan
[10] RIKEN Cluster for Pioneering Research, 2-1, Hirosawa, Wako-shi, Saitama 351-0198, Japan
[11] IGN, Observatorio Astronómico Nacional, Calle Alfonso XII, 28004 Madrid, Spain
[12] Dipartimento di Chimica, Biologia e Biotecnologie, Via Elce di Sotto 8, 06123 Perugia, Italy
[13] LERMA, Université de Cergy-Pontoise, Observatoire de Paris, PSL Research University, CNRS, Sorbonne Université, UPMC, Univ. Paris 06, 95000 Cergy Pontoise, France
[14] National Astronomical Observatory of China, Datun Road 20, Chaoyang, Beijing 100012, PR China
[15] CAS Key Laboratory of FAST, NAOC, Chinese Academy of Sciences, Beijing, PR China
[16] Department of Physics and Astronomy, University College London, Gower Street, London, WC1E 6BT, UK
[17] University of AL-Muthanna, College of Science, Physics Department, AL-Muthanna, Iraq
[18] Centro de Astrobiología (CSIC, INTA), Ctra. de Ajalvir, km. 4, Torrejón de Ardoz, 28850 Madrid, Spain
[19] Ural Federal University, 620002, 19 Mira street, Yekaterinburg, Russia
[20] Departament de Química, Universitat Autònoma de Barcelona, 08193 Bellaterra, Catalonia, Spain
[21] Univ. Rennes, CNRS, IPR (Institut de Physique de Rennes) – UMR 6251, 35000 Rennes, France
[22] ESO, Karl Schwarzchild Srt. 2, 85478 Garching bei München, Germany
[23] Aix–Marseille Université, PIIM UMR-CNRS 7345, 13397 Marseille, France
[24] Università degli Studi di Torino, Dipartimento Chimica Via Pietro Giuria 7, 10125 Torino, Italy
[25] Engineering Research Institute Ventspils International Radio Astronomy Centre of Ventspils University of Applied Sciences, Inženieru 101, Ventspils LV-3601, Latvia

Appendix A: Intensity maps

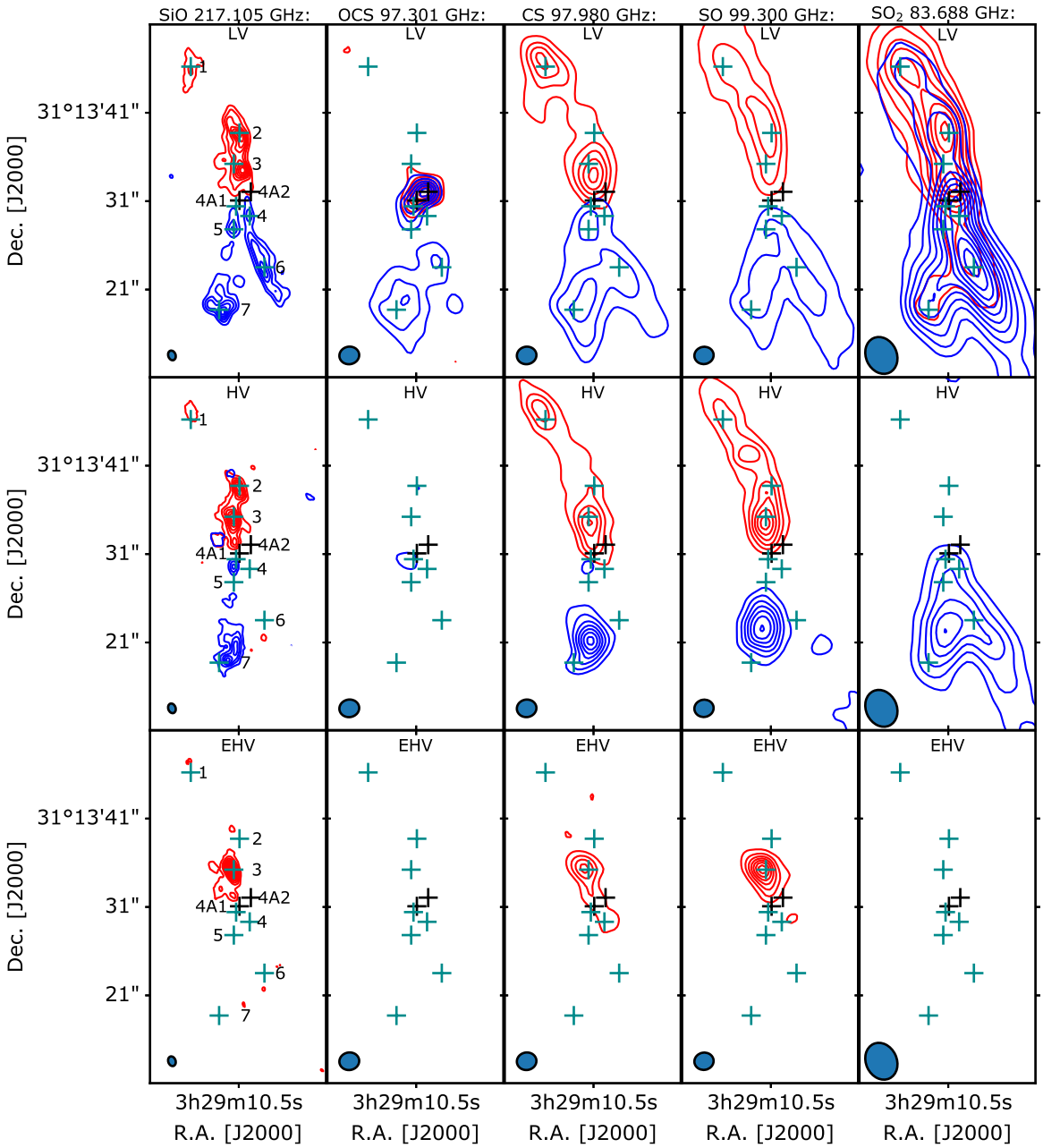


Fig. A.1. Channel maps of the main sulfuretted isotopologues observed at low (∼2–4″) resolution for three velocity ranges: low-velocity LV (−10, +5) and (+10, +25) km s^{-1}, high-velocity HV (−20, −11) and (+26, +40) km s^{-1}, and extremely-high-velocity EHV (−35, −21) and (+41, +55) km s^{-1}.

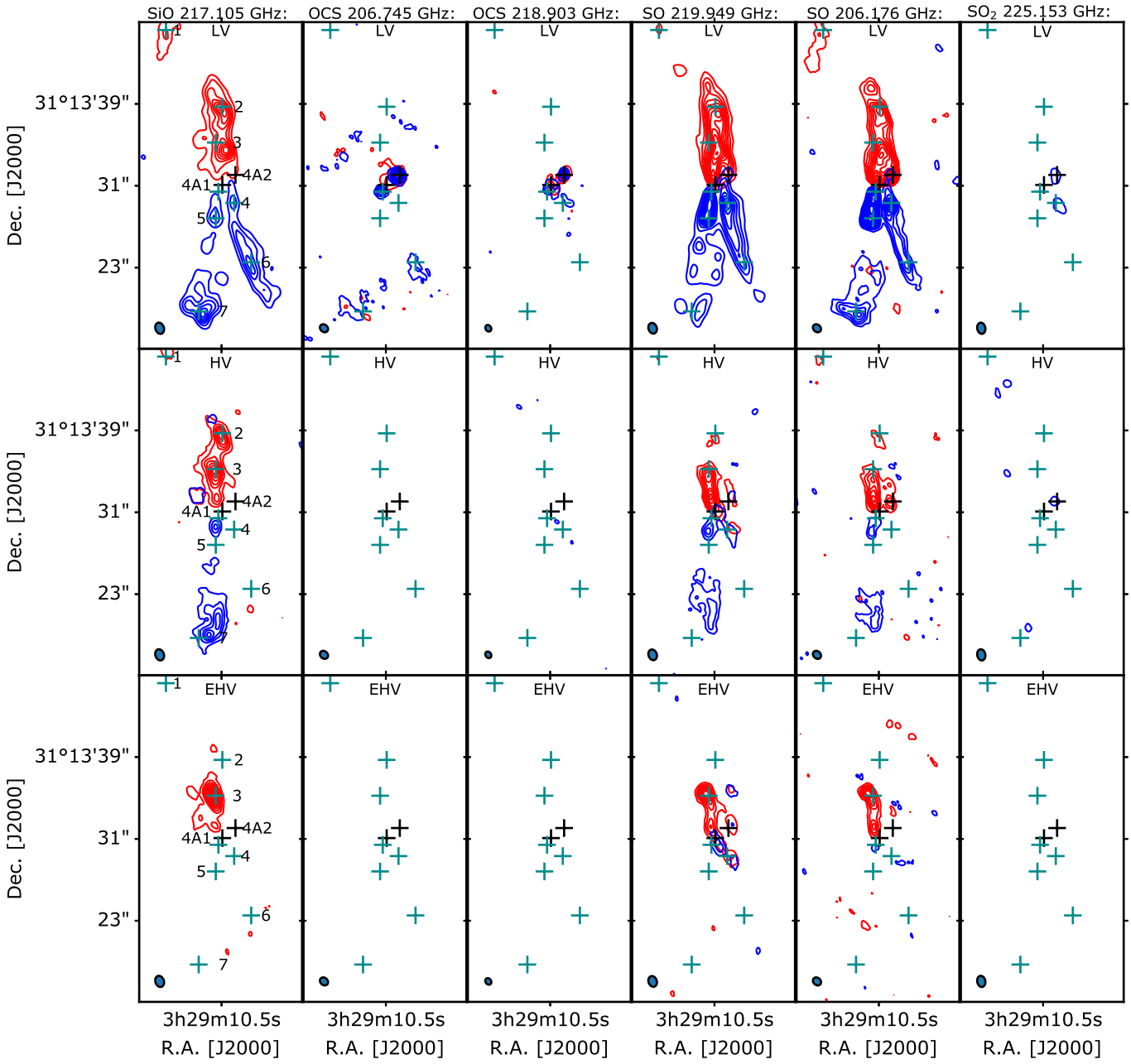


Fig. A.2. Channel maps of the main sulfuretted isotopologues observed at high (∼1″) resolution for three velocity ranges: low-velocity LV (−10, +5) and (+10, +25) km s^{-1}, high-velocity HV (−20, −11) and (+26, +40) km s^{-1}, and extremely-high-velocity EHV (−35, −21) and (+41, +55) km s^{-1}.

Appendix B: Spectra towards SiO and OCS peaks

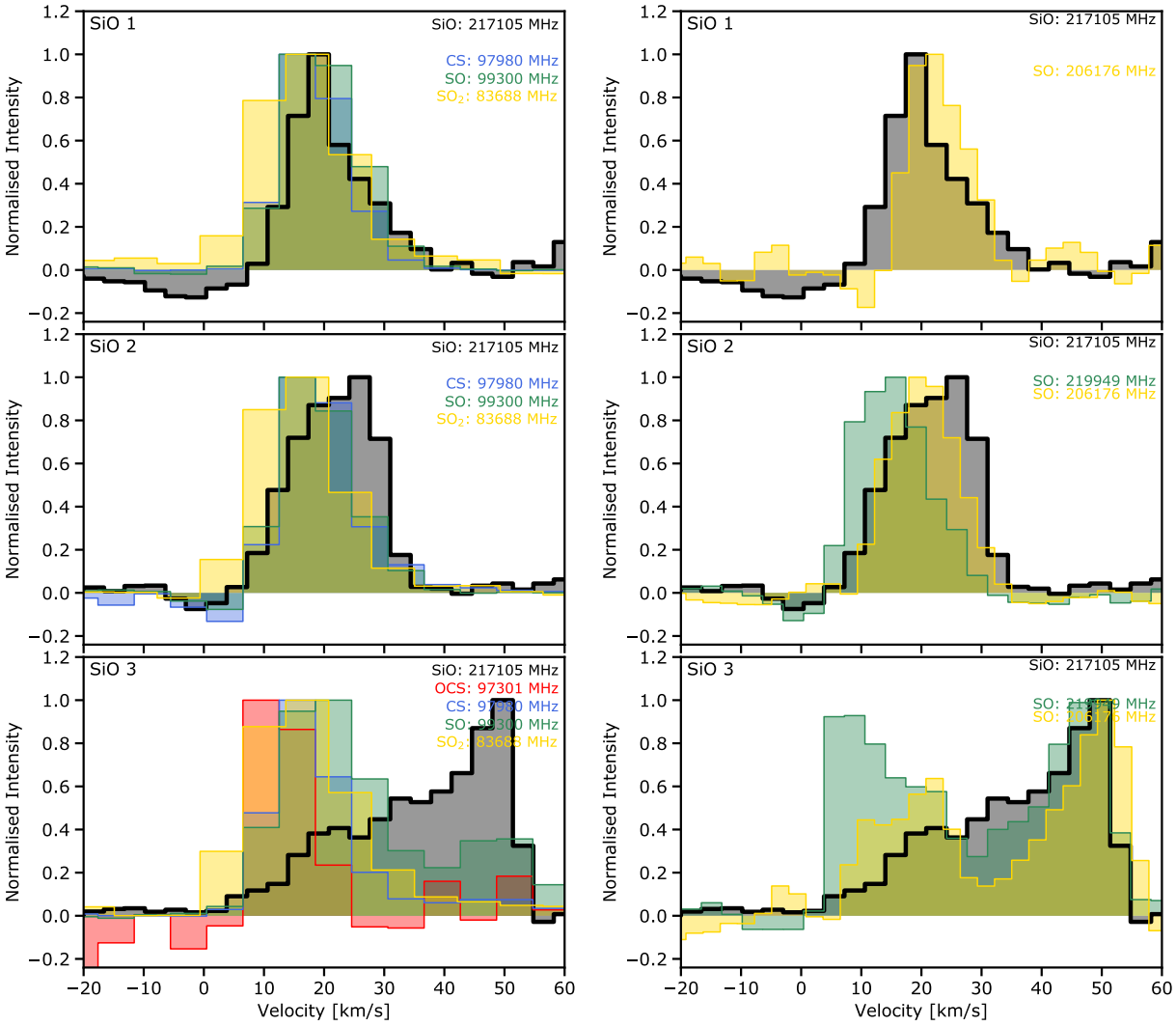


Fig. B.1. Normalised spectra of sulfuretted transitions observed at low (*left panels*) and high (*right panels*) angular resolution compared with the normalised SiO spectra at high angular resolution towards the SiO peaks in the north from IRAS4A if the intensity peak is higher than three times the σ rms noise level.

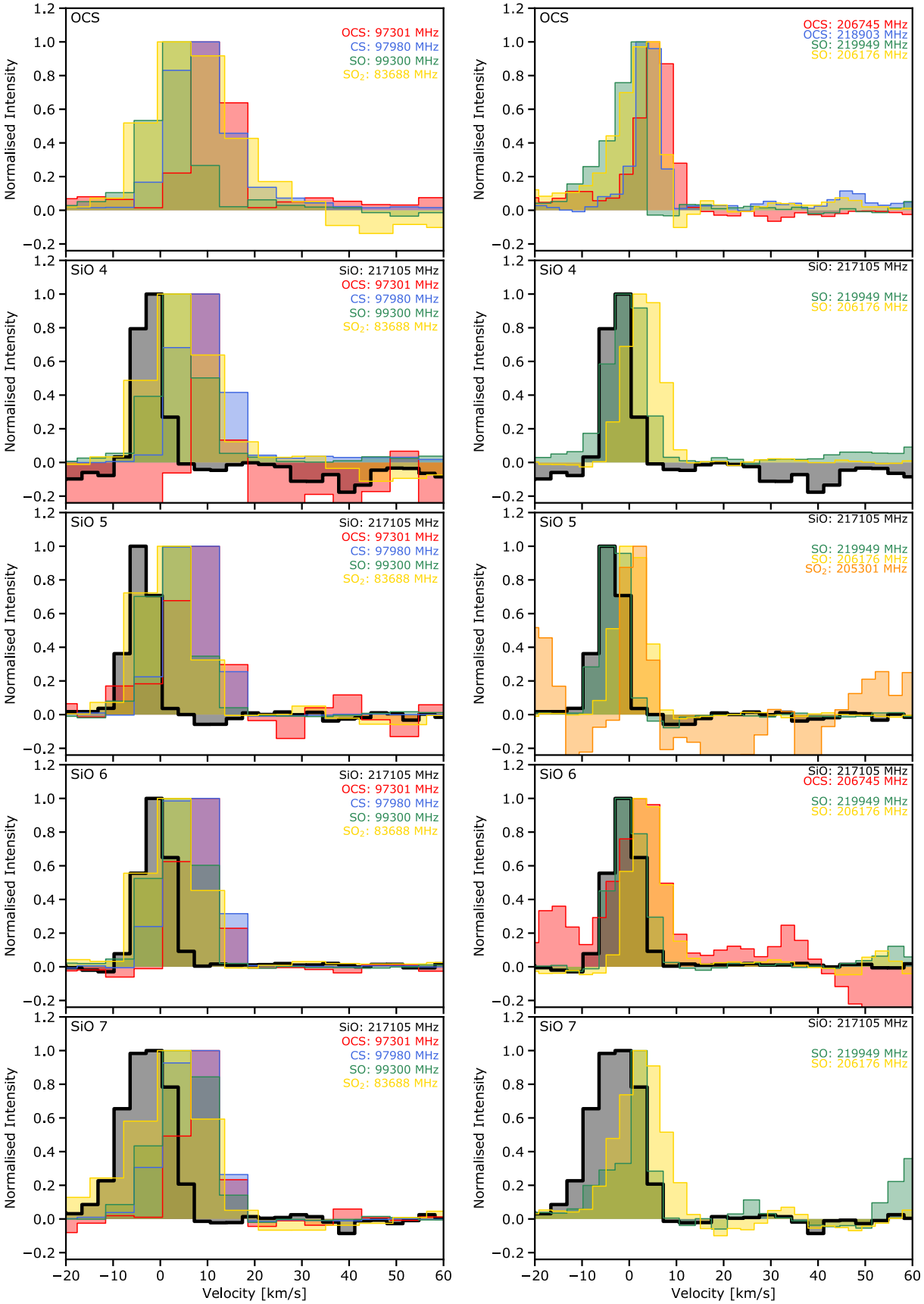


Fig. B.2. Normalised spectra of sulfuretted transitions observed at low (*left panels*) and high (*right panels*) angular resolution compared with the normalised SiO spectra at high angular resolution towards the SiO peaks and the OCS peak in the south from IRAS4A if the intensity peak is higher than three times the σ rms noise level.

Appendix C: Comparison between IRAM-30 m and NOEMA spectra

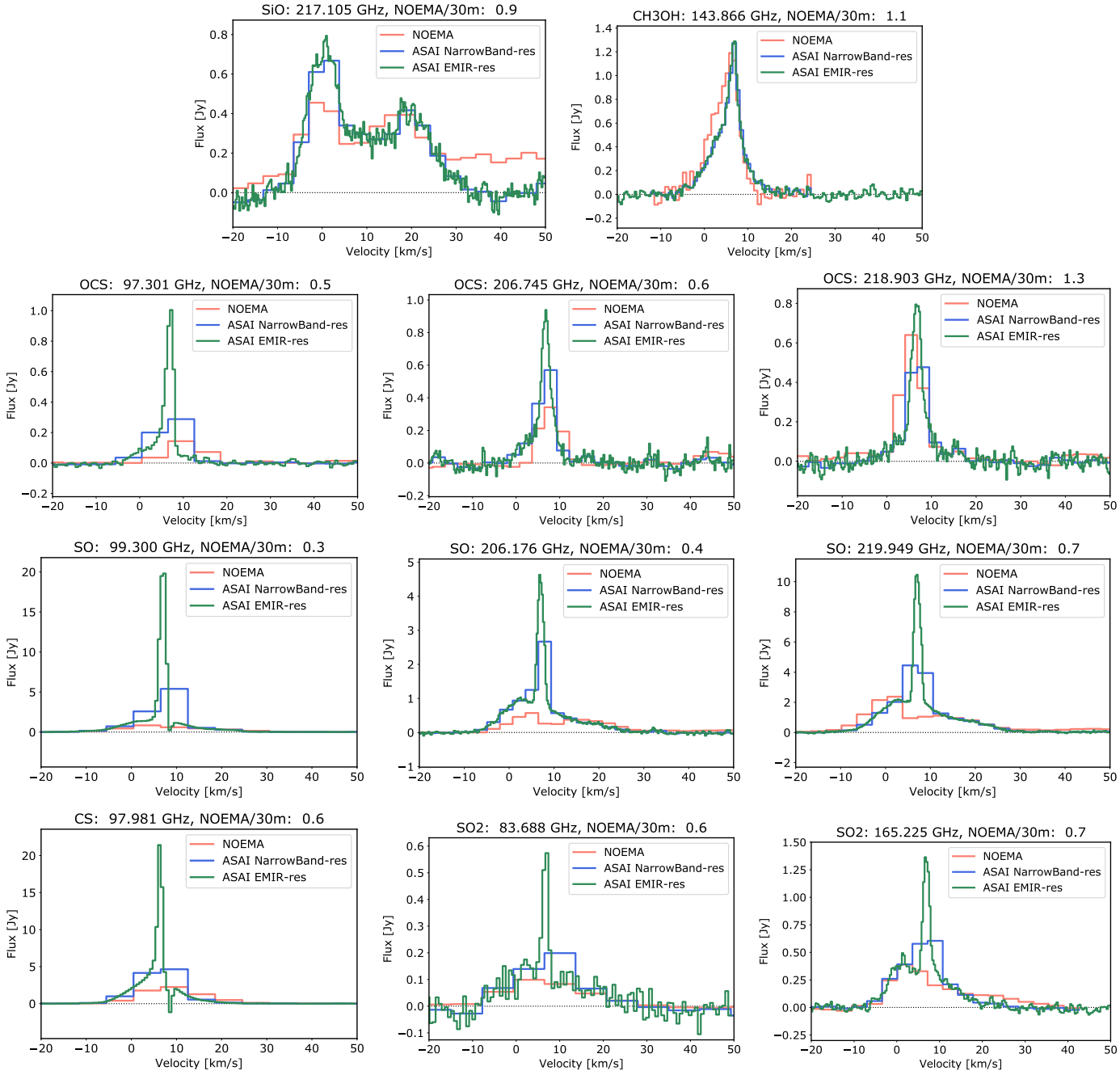


Fig. C.1. Flux spectra of selected species observed with the IRAM-30 m with the ASAI Large Program with the EMIR spectral resolution (in green) and smoothed over the WIDEX resolution (in blue) and with the NOEMA interferometer assuming a mask equal to the IRAM-30 m beam (in red). The CH_3OH transition has been observed with the NOEMA narrow band backend, the spectrum is here shown at a spectral resolution of 0.4 MHz (0.8 km s^{-1}). The flux recovered by NOEMA is reported on top of each panel (see text in Sect. 3.4 for more details).